

Special Section:

The Curiosity rover's investigation of Glen Torridon and the surrounding area

Key Points:

- Sedimentary facies observed by *Curiosity* suggest lacustrine and fluvial environments preserved in the Glen Torridon (GT) stratigraphy
- A paleoenvironmental transition is observed across the Jura/Knockfarril Hill members boundary, suggesting onset of fluvial conditions
- This transition is progressive, and consistent within both the sedimentary and geochemical signals in the GT region

Supporting Information:

Supporting Information may be found in the online version of this article.

Correspondence to:

G. Caravaca,
gwenael.caravaca@irap.omp.eu

Citation:

Caravaca, G., Mangold, N., Dehouck, E., Schieber, J., Zaugg, L., Bryk, A. B., et al. (2022). From lake to river: Documenting an environmental transition across the Jura/Knockfarril Hill members boundary in the Glen Torridon region of Gale crater (Mars). *Journal of Geophysical Research: Planets*, 127, e2021JE007093. <https://doi.org/10.1029/2021JE007093>














Received 14 OCT 2021

Accepted 12 APR 2022

Author Contributions:

Conceptualization: Gwénaél Caravaca, Nicolas Mangold
Data curation: Erwin Dehouck, Alexander B. Bryk, Christopher M. Fedo,

From Lake to River: Documenting an Environmental Transition Across the Jura/Knockfarril Hill Members Boundary in the Glen Torridon Region of Gale Crater (Mars)

Gwénaél Caravaca^{1,2,3} , Nicolas Mangold² , Erwin Dehouck⁴ , Juergen Schieber⁵, Louis Zaugg² , Alexander B. Bryk⁶ , Christopher M. Fedo⁷ , Stéphane Le Mouélic² , Laetitia Le Deit², Steven G. Banham⁸ , Sanjeev Gupta⁸, Agnès Cousin¹ , William Rapin¹, Olivier Gasnault¹ , Frances Rivera-Hernández⁹ , Roger C. Wiens¹⁰ , and Nina L. Lanza¹¹ 

¹UMR 5277 CNRS, UPS, CNES Institut de Recherche en Astrophysique et Planétologie, Université Paul Sabatier Toulouse III, Toulouse, France, ²UMR 6112 CNRS Laboratoire de Planétologie et Géosciences, Nantes Université, Université d'Angers, Nantes, France, ³Now at Institut de Recherche en Astrophysique et Planétologie, Toulouse, France, ⁴Université de Lyon, UCBL, ENSL, UJM, CNRS, LGL-TPE, Villeurbanne, France, ⁵Department of Geological Sciences, Indiana University Bloomington, Bloomington, IN, USA, ⁶University of California Berkeley, Berkeley, CA, USA, ⁷Department of Earth & Planetary Sciences, University of Tennessee, Knoxville, TN, USA, ⁸Department of Earth Sciences and Engineering, Imperial College London, London, UK, ⁹Department of Earth and Atmospheric Sciences, Georgia Institute of Technology, Atlanta, GA, USA, ¹⁰Earth, Atmospheric, and Planetary Sciences, Purdue University, West Lafayette, IN, USA, ¹¹Los Alamos National Laboratory, Los Alamos, NM, USA

Abstract Between January 2019 and January 2021, the Mars Science Laboratory team explored the Glen Torridon (GT) region in Gale crater (Mars), known for its orbital detection of clay minerals. Mastcam, Mars Hand Lens Imager, and ChemCam data are used in an integrated sedimentological and geochemical study to characterize the Jura member of the upper Murray formation and the Knockfarril Hill member of the overlying Carolyn Shoemaker formation in northern GT. The studied strata show a progressive transition represented by interfingering beds of fine-grained, recessive mudstones of the Jura member and coarser-grained, cross-stratified sandstones attributed to the Knockfarril Hill member. Whereas the former are interpreted as lacustrine deposits, the latter are interpreted as predominantly fluvial deposits. The geochemical composition seen by the ChemCam instrument show K₂O-rich mudstones (~1–2 wt.%) versus MgO-rich sandstones (>6 wt.%), relative to the average composition of the underlying Murray formation. We document consistent sedimentary and geochemical data sets showing that low-energy mudstones of the Jura member are associated with the K-rich endmember, and that high-energy cross-stratified sandstones of the Knockfarril Hill member are associated with the Mg-rich endmember, regardless of stratigraphic position. The Jura to Knockfarril Hill transition therefore marks a significant paleoenvironmental change, where a long-lived and comparatively quiescent lacustrine setting progressively changes into a more energetic fluvial setting, as a consequence of shoreline regression due to either increased sediment supply or lake-level drop.

Plain Language Summary Between January 2019 and January 2021, the Mars Science Laboratory team explored the Glen Torridon region in Gale crater. This region is also known as the “clay-bearing unit” after the previous observation of strong spectral signatures of such minerals from orbit. As this indicates the presence of wetter conditions during the Martian past, this area was a main objective of the mission. There, sedimentary strata show a major change from fine-grained mudstones, characteristic of the underlying Murray formation (lake deposits), toward coarser-grained cross-stratified sandstones of the Knockfarril Hill member (river deposits). This change is also identified in the geochemical signal, by the ChemCam instrument. ChemCam data show higher magnesium and lower potassium in the coarse-grained fraction compared to the fine-grained sediment. We also observe a progressive transition with interbedding of both lithologies across the region. We interpret these strata to record a progressive transition from a quiet lake toward a more energetic lake shore to river plain, consequently to shoreline migration, due to either sedimentary fill of the basin and/or a drop in lake level.

© 2022. The Authors.

This is an open access article under the terms of the [Creative Commons Attribution-NonCommercial-NoDerivs License](https://creativecommons.org/licenses/by-nc-nd/4.0/), which permits use and distribution in any medium, provided the original work is properly cited, the use is non-commercial and no modifications or adaptations are made.

Agnès Cousin, Olivier Gasnault, Roger C. Wiens, Nina L. Lanza

Formal analysis: Gwénaél Caravaca, Nicolas Mangold, Erwin Dehouck, Juergen Schieber, Louis Zaugg

Funding acquisition: Olivier Gasnault, Roger C. Wiens, Nina L. Lanza

Investigation: Gwénaél Caravaca, Nicolas Mangold, Erwin Dehouck, Juergen Schieber, Louis Zaugg, Stéphane Le Mouélic, Laetitia Le Deit, William Rapin

Methodology: Gwénaél Caravaca, Nicolas Mangold, Erwin Dehouck, Juergen Schieber, Stéphane Le Mouélic, Frances Rivera-Hernández

Project Administration: Nicolas Mangold, Olivier Gasnault, Roger C. Wiens, Nina L. Lanza

Resources: Alexander B. Bryk, Christopher M. Fedo

Software: Gwénaél Caravaca, Erwin Dehouck, Louis Zaugg, Stéphane Le Mouélic, Olivier Gasnault

Supervision: Nicolas Mangold

Validation: Gwénaél Caravaca, Nicolas Mangold, Erwin Dehouck, Juergen Schieber, Steven G. Banham, Sanjeev Gupta, Agnès Cousin, William Rapin, Frances Rivera-Hernández

Visualization: Gwénaél Caravaca, Erwin Dehouck, Louis Zaugg, Alexander B. Bryk, Christopher M. Fedo

Writing – original draft: Gwénaél Caravaca, Nicolas Mangold, Erwin Dehouck, Juergen Schieber

Writing – review & editing: Gwénaél Caravaca, Nicolas Mangold, Erwin Dehouck, Juergen Schieber, Stéphane Le Mouélic, Laetitia Le Deit, Steven G. Banham

1. Introduction

Gale crater, a ~ 3.7 Ga-old impact crater close to the Martian crustal dichotomy, was selected as the landing site of the Mars Science Laboratory (MSL) mission on the strength of well-expressed sedimentary successions visible from orbit, and spectral data (Compact Reconnaissance Imaging Spectrometer for Mars) that indicated secular mineralogical changes in the strata exposed on the northern flank of Aeolis Mons (informally named Mt Sharp, Figure 1a; Grotzinger, Crisp, et al., 2012; Golombek et al., 2012; Milliken et al., 2010).

Since August 2012, the MSL rover *Curiosity* has explored the northern part of Gale crater to seek out geological evidence for ancient habitable environments (Grotzinger, Crisp, et al., 2012). For ~ 9 years, the MSL team has documented a wide range of siliciclastic rocks that attest to the presence of fluvial, lacustrine, and aeolian depositional settings in the Mt Sharp sedimentary succession (e.g., Banham et al., 2018; Bristow et al., 2018; Edgar et al., 2020; Grotzinger et al., 2015, 2014; Le Deit et al., 2016; Mangold et al., 2015; Rice et al., 2017; Rivera-Hernández et al., 2019; Schieber, Bish, et al., 2017; Schieber, Stein, et al., 2017; Stack et al., 2016; Stein et al., 2018). Documenting past aqueous conditions is important with regard to past habitability and particularly the identification of lacustrine sediments with their inherent tendency to concentrate and preserve organic matter within clay-bearing deposits (e.g., Farmer & Des Marais, 1999; Hays et al., 2017; Summons et al., 2011).

The Glen Torridon (GT) campaign (Bennett et al., 2022) is focused on the area where the strongest clay signatures were detected from orbit (Milliken et al., 2010). Specific objectives of this campaign were lithologies and facies at GT because these strata are lateral equivalents to the Vera Rubin ridge (VRR; Figure 1b), a prominent ridge of lacustrine strata that has undergone substantial diagenetic alteration (e.g., David et al., 2020; Edgar et al., 2020; Fraeman et al., 2020; Frydenvang et al., 2020; L'Haridon et al., 2018, 2020). Because this alteration likely obliterated primary organic matter, it was of critical importance to study their potentially less modified equivalents at GT. In this study, we use the instruments on *Curiosity* at several key locations in GT to document the sedimentary architecture, lithologies, and facies of the exposed strata and the geochemical composition of this material as analyzed by the ChemCam instrument. Careful examination of facies and chemical changes allow us to identify marked lateral and vertical variations of depositional setting across the Jura to Knockfarril Hill transition in GT.

2. Geological Context and Studied Area

Gale crater is ~ 155 km wide (Figure 1a) and formed ca. 3.7 ± 0.1 Ga (Le Deit et al., 2013; Thomson et al., 2011), close to the Noachian-Hesperian transition. It is located at 5.3°S , 137.8°E , near the Martian dichotomy boundary that juxtaposes the highly cratered southern highlands and the smoother northern lowlands. Gale crater belongs to a class of impact craters with thick sedimentary fills (e.g., Bennett & Bell, 2016; Day et al., 2016; Grotzinger, Milliken, & SEPM (Society for Sedimentary Geology), 2012; Malin & Edgett, 2000). It contains a central mound (Mt Sharp, Figures 1a and 1b), that consists of a thick stack of sediments (~ 5 km) that are thought to have been deposited shortly after the crater's formation and continuing into the Hesperian and possibly the Amazonian (Le Deit et al., 2013; Palucis et al., 2014; Thomson et al., 2011). Initially investigated from orbit, the mound records a varied history of ancient sedimentary processes and conditions (e.g., Cabrol et al., 1999; Malin & Edgett, 2000; Milliken et al., 2014, 2010; Rossi et al., 2008; Thomson et al., 2011). Since the arrival of *Curiosity* on 6 August 2012, the MSL team has examined the crater floor along more than 27 kms of traverse from the northern crater floor plain (Aeolis Palus, Figure 1b) to the lower reaches of Mt Sharp (Figure 1b). A synthetic stratigraphic column based on vertical elevation has been prepared by the MSL Sedimentology and Stratigraphy Working Group (Figure 2) to provide a representation of the vertical succession of sedimentary rocks encountered by the rover at specific elevations along the traverse. This column therefore does not indicate a true stratigraphic succession at a given specific location but proffers a representative log of the strata that form Mt. Sharp over more than 10 km of lateral distance, under the assumption of a nearly horizontal stacking pattern (cf., Fedo et al., 2022).

The southward traverse from the Bradbury landing site to the foothills of Mt Sharp (sol 750; Figure 1b) largely crossed fluvial conglomerates and sandstones (e.g., Edgar et al., 2018; Mangold et al., 2016; Rice et al., 2017; Stack et al., 2016; Vasavada et al., 2014) as well as lacustrine deposits (e.g., Grotzinger et al., 2015, 2014; Schieber, Bish, et al., 2017; Schieber, Stein, et al., 2017). Arriving at the Pahrump Hills region (Figure 1b), the rover encountered the first deposits that are clearly part of the Mt Sharp strata. These rocks form the base of the Murray formation and are interpreted as lacustrine on the basis of fine-grained laminated mudstones, similar to those observed on Earth (e.g., Edgar et al., 2020; Grotzinger et al., 2015; Kah et al., 2018; Rivera-Hernández

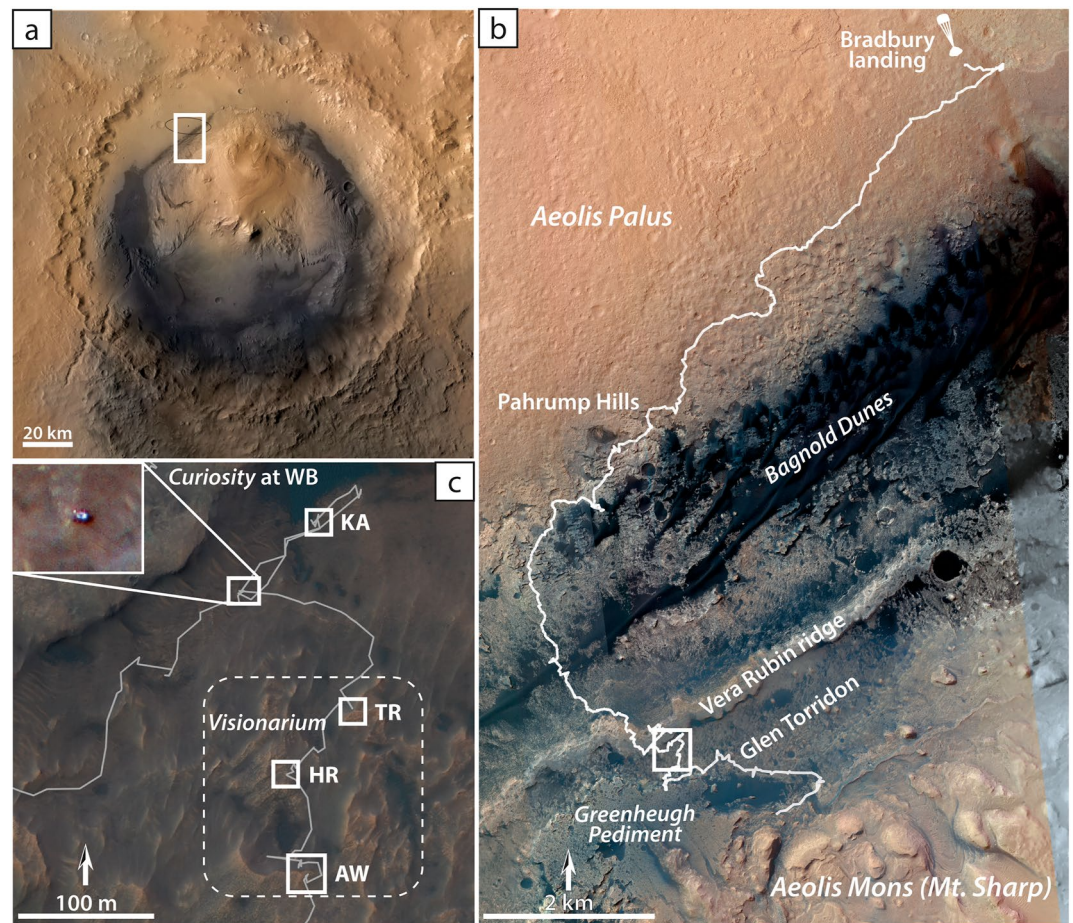


Figure 1. (a) Location of the study area. The white box represents the area of operations of the Mars Science Laboratory rover *Curiosity* in northern Gale crater. (b) The rover traverse (white line) from Bradbury landing and to Glen Torridon (as of June 2021). (c) Study area and location of the selected outcrops along the traverse in northern Glen Torridon. The upper left inset shows the *Curiosity* rover at Woodland Bay from orbit (HiRISE image ESP_060207_1750). The dashed white line delimits the “Visionarium” area. WB: Woodland Bay, KA: Kilmalie/Aberlady drill sites, TR: Teal Ridge, HR: Harlaw rise, and AW: Antonine Wall and Glen Etive drill site.

et al., 2019; Schieber et al., 2015; Stack et al., 2019). At present, interpreted sedimentary environments range from a succession dominated by hyperpycnal flows (Stack et al., 2019) to one that is characterized by saline and hypersaline waters and evaporitic conditions (Kah et al., 2018; Schieber et al., 2015).

After leaving the Pahrump Hills region (~sol 950–1800), the rover traversed a thick succession of Murray formation strata (350+ m elevation change, Figure 2) up to the base of the VRR. Being of considerable variability, these strata are currently considered a reflection of dominantly lacustrine deposition and highly variable lake levels (Edgar et al., 2020; Fedo et al., 2017; Schieber, Bish, et al., 2017; Schieber, Stein, et al., 2017; Stein et al., 2018). The interval consists largely of mudstones of the Pahrump Hills, Karasburg, Sutton Island, and Blunts Point members (Figure 2). Coarser-grained strata (sandstones) have been described from the Hartmann's Valley and the Pettegrove Point members (Figure 2; e.g., Edgar et al., 2020), and may indicate episodic changes in local depositional settings, possibly due to aeolian or fluvial incursions in a lake margin setting (e.g., Edgar et al., 2020; Gwizd et al., 2018, 2019). Such episodic but important shifts in the local depositional conditions probably occurred at multiple points in Murray formation history, as indicated by lowstand deposits (Schieber, Bish, et al., 2017; Schieber, Stein, et al., 2017), desiccation cracks (Stein et al., 2018), and hypersaline interludes (Rapin et al., 2019).

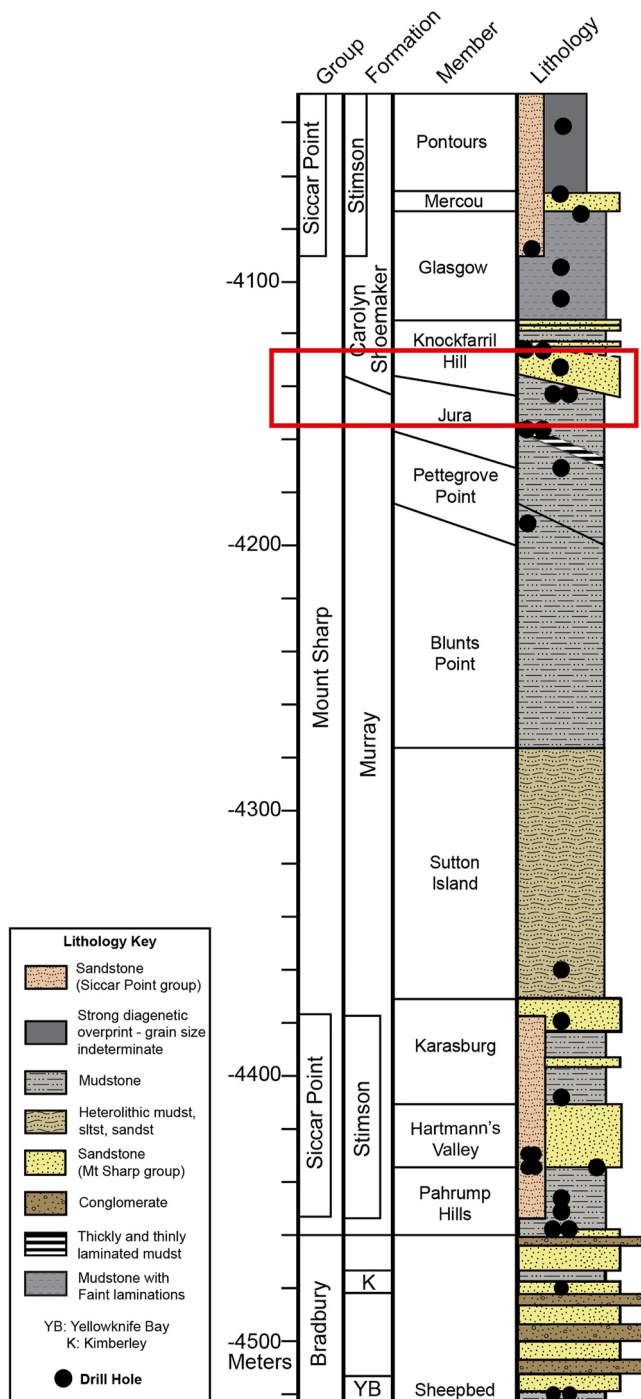


Figure 2. Synthetic stratigraphic column of the region explored by *Curiosity* (after Fedo et al., 2022). The column illustrates the variety of deposits encountered by the rover at the elevation range they were observed, from coarse fluvio-deltaic sandstones to conglomerates in the Bradbury Group, to finer mudstones of lacustrine origin in the Murray formation and to the fluvial sandstones of the Carolyn Shoemaker formation. The aeolian sandstones of the Stimson formation unconformably overlie the Mount Sharp group at several locations along the traverse. The red box marks the studied interval across the Jura-Knockfarril Hill members boundary. YB: Yellowknife Bay formation. K: Kimberley formation.

Cross-stratified aeolian sandstones of the Stimson formation (Siccar Point group, Figure 2; Banham et al., 2018, 2021, 2022; Bedford et al., 2020, 2022) have been observed to unconformably overlie the Murray and Carolyn Shoemaker formations in multiple places and elevations (as denoted by the two non-continuous placements illustrated on the column in Figure 2). They are remnants of an ancient aeolian sediment blanket, comparable to the current-day Bagnold active dune system (Figure 1b). The Stimson formation is thought to be much younger than the Mount Sharp group as a whole (Banham et al., 2018; Fedo et al., 2020, 2022), significantly post-dating the wet and fluvio-lacustrine history of Gale, because it is also observed unconformably overlying the Carolyn Shoemaker formation strata in the Greenheugh Pediment (GP) area, which is located 300 m higher in the stratigraphic succession than its first unconformable iteration encountered at Pahrump Hill (Figures 1b and 2; Banham et al., 2021, 2022; Bedford et al., 2022). The Stimson formation does not crop out in the study area.

From sols ~1800 to ~2300, the rover traversed the VRR, a prominent topographic feature associated with hematite detection in orbital spectra (e.g., Milliken et al., 2010). VRR strata largely consist of mudstones with local intercalations of very fine- to fine-grained sandstones, and include the Blunts Point, Pettegrove Point, and Jura members of the Murray formation. Considered to record lacustrine conditions (Edgar et al., 2020), VRR strata show a complex diagenetic history that led to the formation of various minerals including hematite due to enhanced groundwater circulation and localized pH and/or redox fronts within partly to fully lithified sediments (e.g., David et al., 2020; Fraeman et al., 2020; Frydenvang et al., 2020; L'Haridon et al., 2018, 2020).

From Sol 2300 onward, *Curiosity* commenced detailed exploration of the GT region (Figure 1b). Whereas the initial traverse route (Mount Sharp Ascend Route) was planned along a roughly NW-SE transect, it was amended several times during the campaign to allow a thorough exploration of the broader region from VRR in the North, up to the GP capping unit (Figure 1b) to the South. Several lateral deviations provided a wealth of data to examine lateral variability within GT strata, particularly in the “Visionarium” area (Figure 1c; Bennett et al., 2022; Fedo et al., 2022), a region informally named due to the exceptional “vision” (*sensu* visibility) of strata allowed by the presence of well-developed outcrops. The GT campaign extended for more than 600 sols and resulted in 10 drill samples.

The GT sedimentary record encompasses the Jura member of the Murray formation and the Knockfarril Hill and Glasgow members of the Carolyn Shoemaker formation (Figure 2). These units are composed of mudstones (Jura member; Edgar et al., 2020; Fedo et al., 2020) and very fine- to medium-grained sandstones (Knockfarril Hill and Glasgow members; Fedo et al., 2020, 2022) that are laterally discontinuous. All these deposits contain significant amounts of clay minerals (e.g., Bristow et al., 2021; Cousin et al., 2021; Thorpe et al., 2020), confirming prior detection with orbital spectrometry (e.g., Milliken et al., 2010).

In this study, we focus on the transition between the Jura and Knockfarril Hill members because of the major change in lithology observed in the northern part of GT along this boundary (Figures 1c and 2). Five outcrops from that area have been selected for this study (Figure 1c): Woodland Bay (sols 2414–2427), the Kilmarie/Aberlady drill site (sols 2359–2410), Teal ridge (sols 2440–2447), Harlaw rise (sols 2459–2463), and the Antonine Wall

outcrop, and Glen Etive drill site (sols 2476–2555). Those outcrops are identified by their informal names rather than the sol which they were observed for clarity. A detailed survey of sedimentary and geochemical features was performed for each outcrop, and the list of the individual ChemCam and Mars Hand Lens Imager (MAHLI) targets investigated at and between those five outcrops is tabulated in Table S1.

3. Data, Materials, and Methods

3.1. Instruments and Products

The *Curiosity* rover is equipped with multiple cameras, allowing for a wide range of observations: the Navcam (Navigation Camera) instrument consists of two pairs of greyscale wide-angle stereo cameras (only one pair is used at a time; Maki et al., 2012). The Mastcam (Mast Camera) instrument consists of one pair of full-color high-resolution cameras with filter wheels for multispectral imaging. The two cameras have different focal lengths, 34 and 100 mm for Mastcam left (ML) and right (MR), respectively (Bell et al., 2017; Malin et al., 2010, 2017). The MAHLI instrument is a full-color high-resolution micro-imager positioned at the end of the robotic arm of the rover, able to resolve coarse silt grains ($12\ \mu\text{m}/\text{px}$) from a distance of ~ 2 to ~ 4 cm (Edgett et al., 2012). The RMI (Remote Micro-Imager) is a subsystem of the ChemCam instrument, designed to provide high-resolution greyscale context images of the targets investigated by the ChemCam instrument (Le Mouélic et al., 2015; Maurice et al., 2012; Wiens et al., 2012). In this study, we use various image products to assess the outcrops explored by the rover, and to characterize the exposed rocks, their structures and texture (Mastcam, MAHLI, and RMI); and to compute 3D Digital Outcrop Models (DOMs) of key locations and structures (Navcam, Mastcam, and MAHLI).

Geochemical data are investigated using the ChemCam instrument and its Laser-Induced Breakdown Spectrometer (LIBS). This instrument allows acquisition of elemental composition of individual rock targets up to ~ 7 m of distance (effective range usually between 2 and 3 m; Maurice et al., 2012; Wiens et al., 2012, 2021). LIBS measurements are performed by firing a short laser pulse at the rock target to create a plasma. When the excited ions cool, the emitted light is analyzed to determine the abundance of major rock-forming oxides (SiO_2 , TiO_2 , Al_2O_3 , FeO , MgO , CaO , Na_2O , and K_2O ; Clegg et al., 2017; Wiens et al., 2013) and select minor elements (e.g., Li, Sr, Ru; Ollila et al., 2014; Payré et al., 2017), with all iron content reported as FeO . In this study, we focus on the analysis of 36 ChemCam targets from the Woodland Bay, Teal ridge, Harlaw rise, and Antonine Wall sites mentioned above (Table S1). Only bedrock analyses are considered (soils, diagenetic veins, etc. have been excluded). For this work we focus on specific oxides (SiO_2 , MgO , CaO , Na_2O , and K_2O) to be used as geochemical markers characteristic of the sedimentary facies. In-depth analyses of the bulk bedrock geochemistry performed in the GT region are detailed in the companion work by Dehouck et al. (2022) and also in Gasda et al. (2022).

3.2. Digital Outcrop Modeling

The various scales provided by the different cameras (from several μm per pixel and up to several cm per pixel) are helpful in observing multiple different levels of detail within the sedimentary architecture and allow multi-scale interpretation of the outcrops. To understand sedimentary architecture and spatial association of sedimentary structures, 3D reconstructions of outcrops and specific targets were done with Structure-from-Motion photogrammetry (Ullman, 1979). This technique is particularly suited to accurately recreate the 3D shape of geological objects of varying sizes using a set of overlapping images (e.g., Caravaca et al., 2020; Le Mouélic et al., 2020; Tavani et al., 2014; Triantafyllou et al., 2019; Verhoeven, 2011; Westoby et al., 2012). Whereas the photogrammetric reconstruction process is complex due to varying optical parameters of the rover's instruments (as discussed by Caravaca et al., 2020), we are nevertheless able to reconstruct both outcrops and individual targets to fit our needs for close inspection and reconstruction of architectural geometry.

The DOMs were computed using Agisoft Metashape Professional software (v.1.6; Agisoft LLC, 2020), whose embedded geospatial features also allow the scaling of the models and enable us to make accurate size measurements on the DOMs. We used the CloudCompare software (v.2.10; Girardeau-Montaut, 2020) for other 3D-related tasks (validation of the scale and visualization). Several of these DOMs were integrated within a game engine to enable true-scale visualization of the structures within a Virtual Reality system (e.g., Caravaca et al., 2020; Le Mouélic et al., 2018, 2020). As a complement, we also used the NASA-developed Augmented

Reality application OnSight (Abercrombie et al., 2017). This allows users to observe positions of the scientific targets within a terrain reconstruction generated from rover data, which is helpful for contextualizing targets.

3.3. Determination of Key Sedimentary Characteristics

Determination of the size and shape of the sedimentary structures was performed using 2D images from Mastcam (ML or MR) or DOMs produced using Navcam and Mastcam images. Scaling on the 2D Mastcam imagery varies according to target distance, but usually allows observation of sub-cm-scale details on MR images (Malin et al., 2017). Accurate measurement of feature size, and allowing for their spatial orientation, was performed using scaled DOMs (cf., Caravaca et al., 2020). This allowed sub-cm measurement of objects on the 3D models.

Grain size and fine-scale structures (lamination, diagenetic veins, etc.) were visually investigated and characterized using MAHLI and RMI high-resolution images (e.g., Mangold et al., 2016; Stack et al., 2019). MAHLI images were scaled from the instrument standoff distance, resulting in a pixel size varying from ~ 17 to ~ 100 $\mu\text{m}/\text{pixel}$ (for 1–25 cm standoff distance, respectively; Edgett et al., 2020a, 2020b). A similar scaling is performed for the RMI images, resulting in pixel sizes ranging from ~ 40 to ~ 150 $\mu\text{m}/\text{pixels}$ (Le Mouélic et al., 2015). These image data sets are useful in resolving grain size down to coarse silt. Grain size is classified according to Wentworth (1922) and Lazar et al. (2015). In this study, a “mudstone” is a rock composed of more than 50% particles with a grain size of <62.5 μm (Lazar et al., 2015). Lamina thickness was measured using MAHLI 2D images or 3D micro-DOMs derived from MAHLI images. These products allow measurement of sub-mm-scale grains and structures. The laminae thickness was preferentially measured on 3D models to take advantage of the ability to measure orthogonally to the bedding plans. An arithmetic mean of these measurements was calculated for each outcrop and target observed. A complete set of measurements is available in Table S2.

4. Outcrop Characterizations

4.1. Woodland Bay

The Woodland Bay outcrop was first observed during the initial eastward traverse (cf., Figure 1c) on Sol 2357. After the drill campaign at Kilmarie/Aberlady and before entering the Visionarium area to the South (Figure 1c), the rover stopped at this outcrop during Sols 2414–2427 to examine the meter-scale outcrop patches with alternating massive and laminated cm-scale beds (Figure 3a). These heterolithic strata show low-angle truncation surfaces (red lines in Figure 3b) that differentiate them from the surrounding, more massive rocks. Based on the examination of close range MAHLI images, the grain size of these beds is inferred to be in the mudstone/siltstone range (locally up to very fine/fine sandstone). At Woodland Bay several bedding plane exposures show cm-scale polygonal cracks (Figure 3a) that are not observed as distinctly elsewhere in the region (e.g., Figure 4a).

A micro-DOM has been computed on the MAHLI target Morningside (Sol 2424; Figure 3b). On this model, we can observe intercalation of bundles of mm-scale mudstone laminae with cm-scale erosion-resistant mudstone/siltstone beds. Localized occurrences of (very) fine-grained sandstones (e.g., yellow arrow in Figure 3b) are observed, which can be difficult to differentiate from coarse mudstones/siltstones. In the resistant beds, layering is obscured, probably due to cementation, we do observe in the recessive laminated part that layering is wavy-non-parallel (blue lines in Figure 3b), laminae diverge and converge forming small-sized lenticular features (green lines in Figure 3b, green arrows in Figure 3c), and in places show low-angle truncations (red lines in Figure 3b).

The resistant layers show vertical jointing that does not continue into the intervening softer intervals. These are probably the side views of the polygonal fracture networks that these harder layers show on bedding planes.

The thickness of individual laminae has been measured to be $\sim 0.35 \pm 0.06$ mm for the resistant beds, and $\sim 0.63 \pm 0.13$ mm in the recessive intervals.

Collectively, these elements point at two depositional settings at Woodland Bay differing by the energy involved for the deposition. On one hand, massive mudstone beds denote a (very) low energy setting, and on the other hand, the laminated beds would represent more dynamic settings, as on Earth, this lamina geometry typically is associated with ripple lamination. This intricate interbedding of massive and laminated beds suggests that the energy of

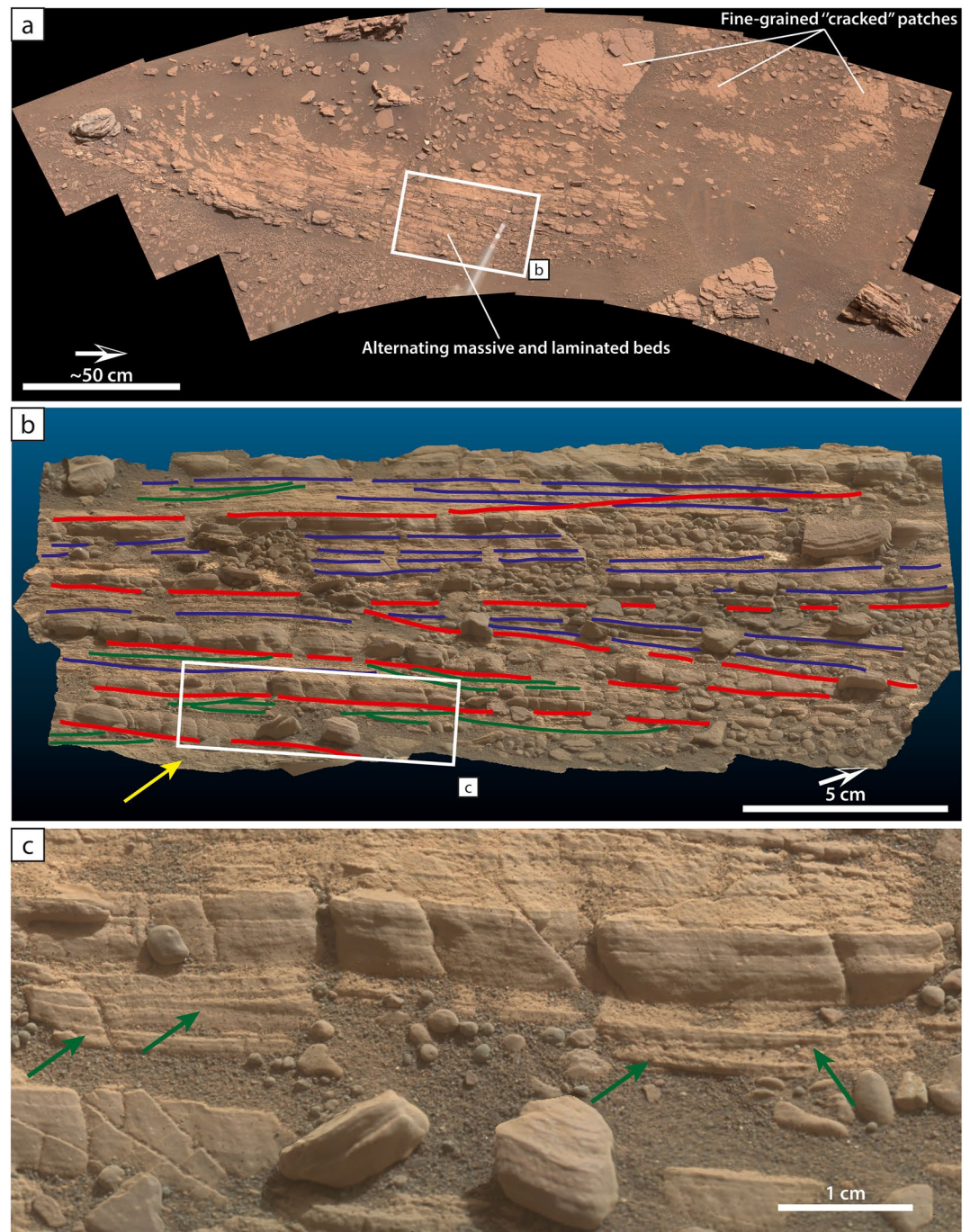


Figure 3. (a) A general view of the Woodland Bay outcrop, showing occurrence of alternating massive and laminated cm-scale coarse mudstones (locally up to fine sandstones), and several exposures of cm-scale polygonal cracks. Mastcam mosaic acquired on Sol 2427 (sequence mcam012854). (b) A view of the micro-Digital Outcrop Model (DOM) of the Morningside target, showing interstratified, thicker, resistant beds with vertical jointing, and more thinly bedded softer intervals (blue lines), as well as low-angle truncation surfaces (red lines). Green lines highlight small-sized lenticular features. The yellow arrow points to a coarse-grained part, possibly up to fine sandstone. Micro-DOM was computed from 16 Mars Hand Lens Imager images taken on Sol 2424; mesh can be viewed on Sketchfab at: <https://skfb.ly/6SE7y>. (c) A detailed view on the converging and diverging laminae (green arrows) forming small-sized lenticular shapes.

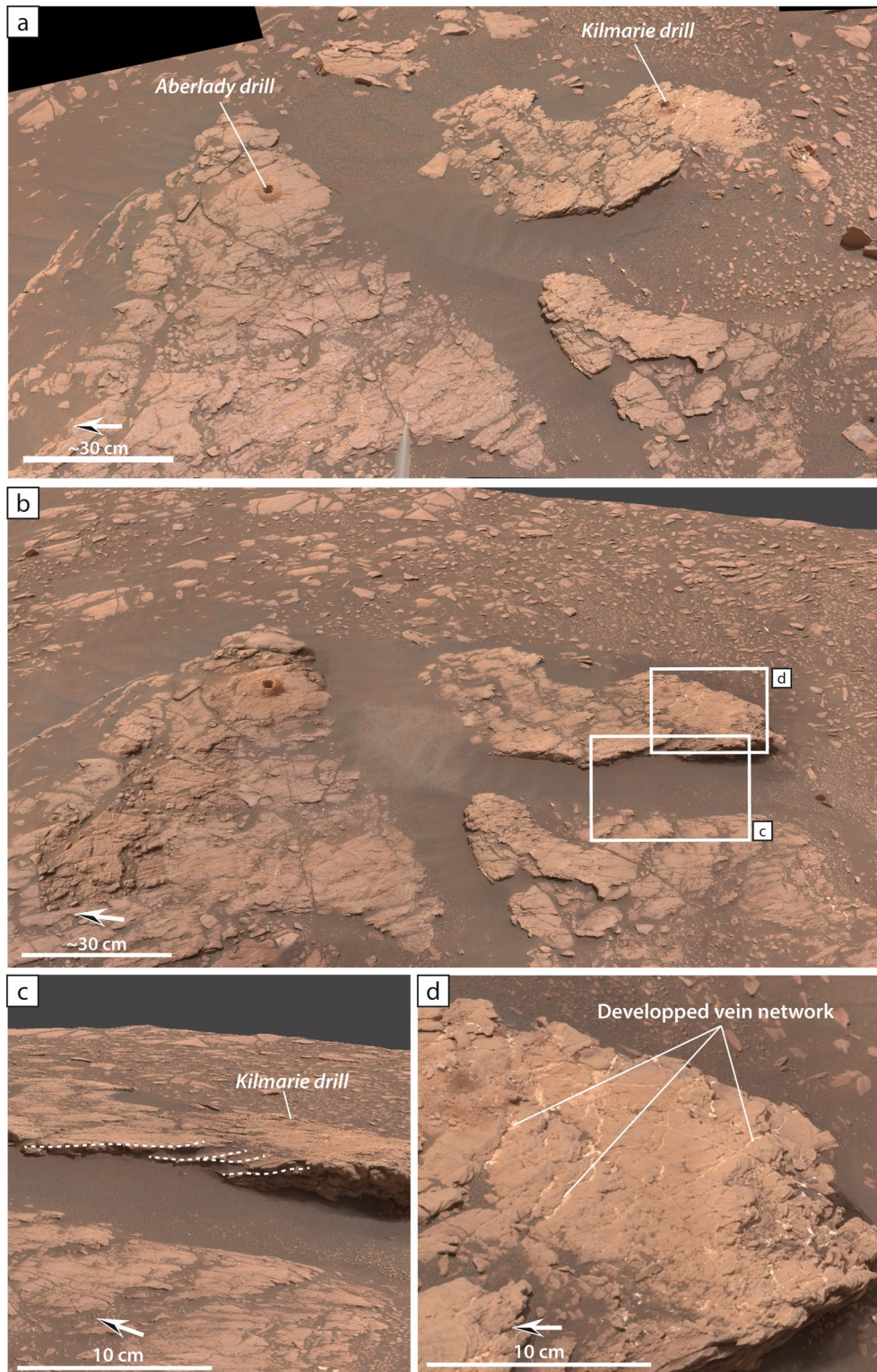


Figure 4. (a) A general view of the Kilmarie/Aberlady drills site, showing the position of each drillhole on their respective resistant slab, cropping out of the surrounding rubbly and smoother terrain. Composite Mastcam mosaic with images acquired on Sol 2371 (sequence mcam012571) and on Sol 2405 (sequence 12753). (b) A general view of the Digital Outcrop Model of the locality computed from 178 Navcam and 732 Mastcam images taken during Sols 2365–2406; mesh visible on Sketchfab at: <https://skfb.ly/ooNz9>. (c) A detailed view of the side of the Kilmarie slab, highlighting the presence of cm-scale cross-stratifications visible in section. (d) Detail of the top of the same slab with visible the laminae terminations on the flat surface. A light-toned vein network can also be observed on this surface.

the setting varied rapidly on a local scale, with alternating lower and seemingly higher energetic conditions. This variation in deposition could also be at the origin of the differential weathering behavior observed here.

4.2. Kilmarie/Aberlady Drill Site

The first drill samples of the GT campaign (Kilmarie and Aberlady) were collected between Sols 2359 and 2410 at an outcrop situated in the northeastern part of the GT area, just below the VRR (cf., Figures 1b, 1c and 4). This outcrop is characterized by the presence of several dm- to meter-scale slabs of erosion-resistant fine- to medium-grained sandstones (Figure 4a). These slabs outcrop up to ~5 cm (Figure 4b) above a rubbly- to smooth-weathering mudstone bedrock which is fractured or covered by regolith.

A DOM has been computed for the drill operations area, with specific focus on the drilled slabs (Figure 4b). In this 3D model, we can observe that the rock slabs occur within a restricted part of the exposure that covers only ~6 m² and is surrounded by smooth weathering mudstone bedrock. The slabs are likely from the same stratum, and in side view they show cm-scale cross-stratification in places (Figure 4c). The dip direction of foresets suggests sediment transport (and current flow) in a northerly direction (Figure 4a). Laminae have a mean thickness of $\sim 0.75 \pm 0.11$ mm and $\sim 1.09 \pm 0.14$ mm on the Kilmarie and Aberlady slabs, respectively. These coarser-grained cross-stratified slabs appear more resistant to erosion than the surrounding rubbly bedrock and host a well-developed network of light-toned veins. They are particularly well developed on the Kilmarie drill slab (Figure 4d).

Collectively, these elements point at a depositional setting dominated by deposition of coarser-grained, cross-strata forming sandstones within condition allowing for a moderately energetic but sustained unidirectional flow.

4.3. Teal Ridge

The Teal ridge locality was one of the first outcrops encountered in the Visionarium area, between Sols 2440 and 2447. This outcrop is one of the best exposures of the Visionarium area, and forms a mesa ~8 m-long and ~1-m-high (Figure 5a). While the mesa is composed of fine- to medium-grained sandstones, the surrounding area is composed of a smoother mudstone bedrock, mostly covered by the regolith. We therefore infer a probable sharp contact between those two lithologies at the base of the Teal Ridge mesa (dashed line in Figure 5a). The rocks composing the mesa have been sculpted out of the surrounding rocks due to their erosion resistance. The central and western part of the mesa (Figure 5a) present a well-preserved cliff-face that allows examination and description of dm- to meter-scale cross-stratification within the sandstones. Some of the structures on the westernmost end of the mesa show a concave base characteristic of a meter-scale channel form (Figure 5b).

For further study of sedimentary features, a DOM of the Teal Ridge outcrop has been computed (Figure 5c). On this model, we see a variety of sedimentary structures within the fine- to medium-grained sandstones, and more particularly the presence of compound crossbedding (Figure 5d). Cross-stratification is seen in dm- to meter-scale bedsets (blue lines in Figure 5d), as well as at the mm- to cm-scale (green lines in Figure 5d). Whereas cross-stratification is already well visible at the macroscale, it can also be observed in close-up images.

For the latter observation, a micro-DOM has been computed on the MAHLI target Stack_of_Glencoul (Sol 2444), situated on the eastern part of the Teal Ridge outcrop (Figures 5c and 6). This DOM (Figure 6b) helps to confirm the original character of small-scale cross-stratification, showing them to be an integral part of the larger scale cross-stratification (Figures 5d and 6a). We observe mm-scale laminations with a mean thickness of 0.61 ± 0.22 mm (blue lines, Figure 6c), organized into at least four bedsets of low angle ($<15^\circ$), cm-scale cross-strata, separated by sharp truncation surfaces (red lines, Figure 6c). The DOM shows apparently opposing transport directions (left to right, from bottom to top in Figure 6c), probably indicating that we observe a plane approximately perpendicular to the transport direction of 3D bedforms. On other parts of the Teal ridge outcrop some layering shows an undulating character, for example, on the Beaully MAHLI target (Sol 2443, Figure S1 in Supporting Information S1). On this target the mean lamina thickness is 0.60 ± 0.14 mm.

No mudstone interval was observed in the Teal ridge section, and most outcropping features seem to be relatively resistant to erosion. Multiple light-toned veins occur throughout the outcrop at the macroscale (Figures 5d and 6a) and at the microscale (Figures 6b and 6c). Some of these veins crosscut the sediment layers, whereas others seem to follow them (Figures 6b and 6c).

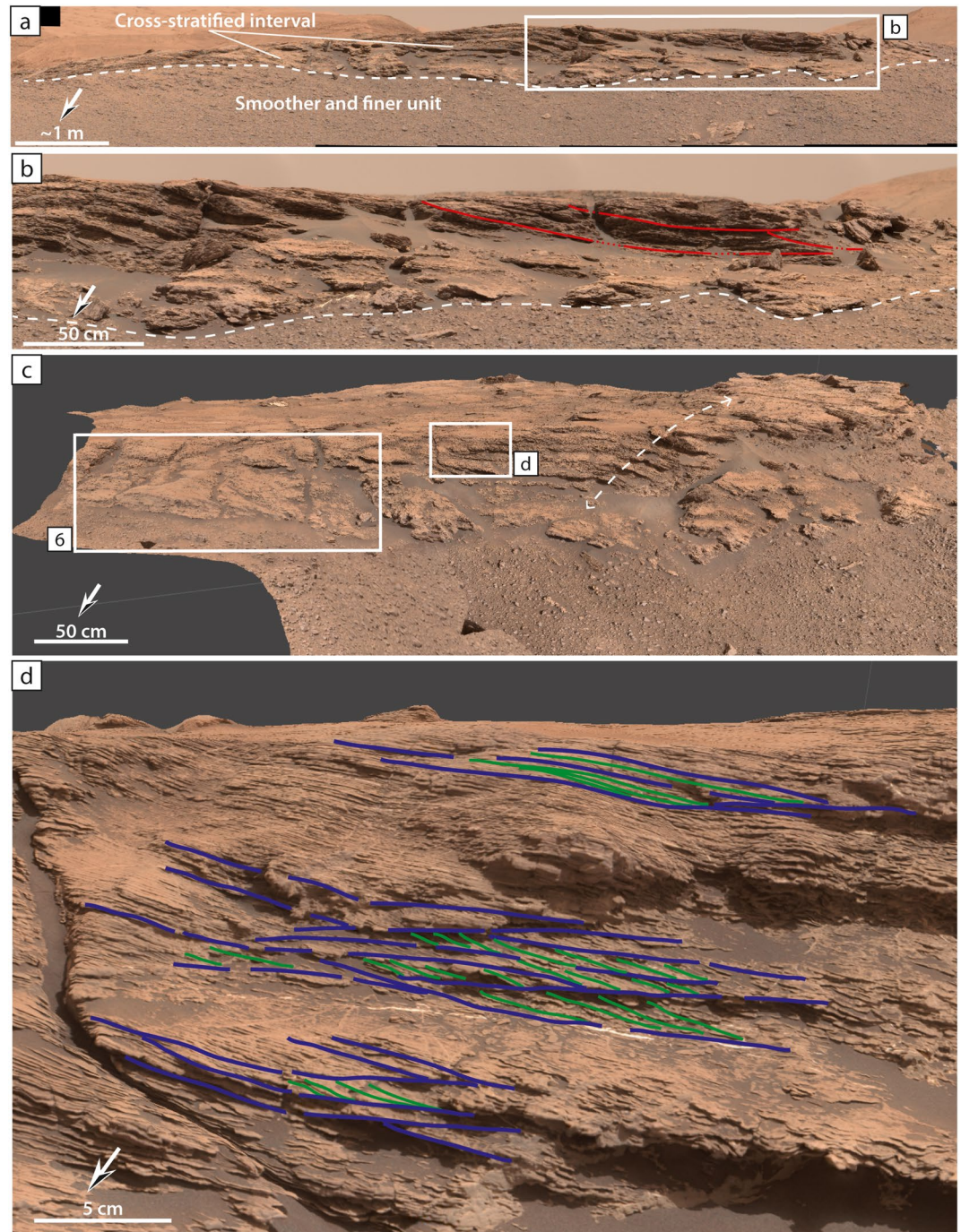


Figure 5. (a) A general view of the Teal ridge outcrop in the Visionarium. Mastcam mosaic acquired on Sol 2435 (sequence mcam12925). The mosaic highlights a continuous exposure of cross-stratified sandstones. The dashed line indicates a probable sharp contact of the sandstones overlying mudstone bedrock. (b) A detailed view of the western part of the outcrop, showing possible meter-scale channel-shapes with concave bases (red lines). (c) A general view of the Digital Outcrop Model (DOM) of the locality, showing the mesa structure of the 8 m long outcrop. Dashed line indicates inferred deformation axis. The DOM was computed from 214 Navcam and 540 Mastcam images taken between Sols 2435 and 2450; mesh visible on Sketchfab at: <https://skfb.ly/opy8r>. (d) A detailed view of the central part of the section, showing compound cross-stratification (blue lines: dm- to meter-scale stratification; green lines: mm- to cm-scale cross-strata within these larger beds).

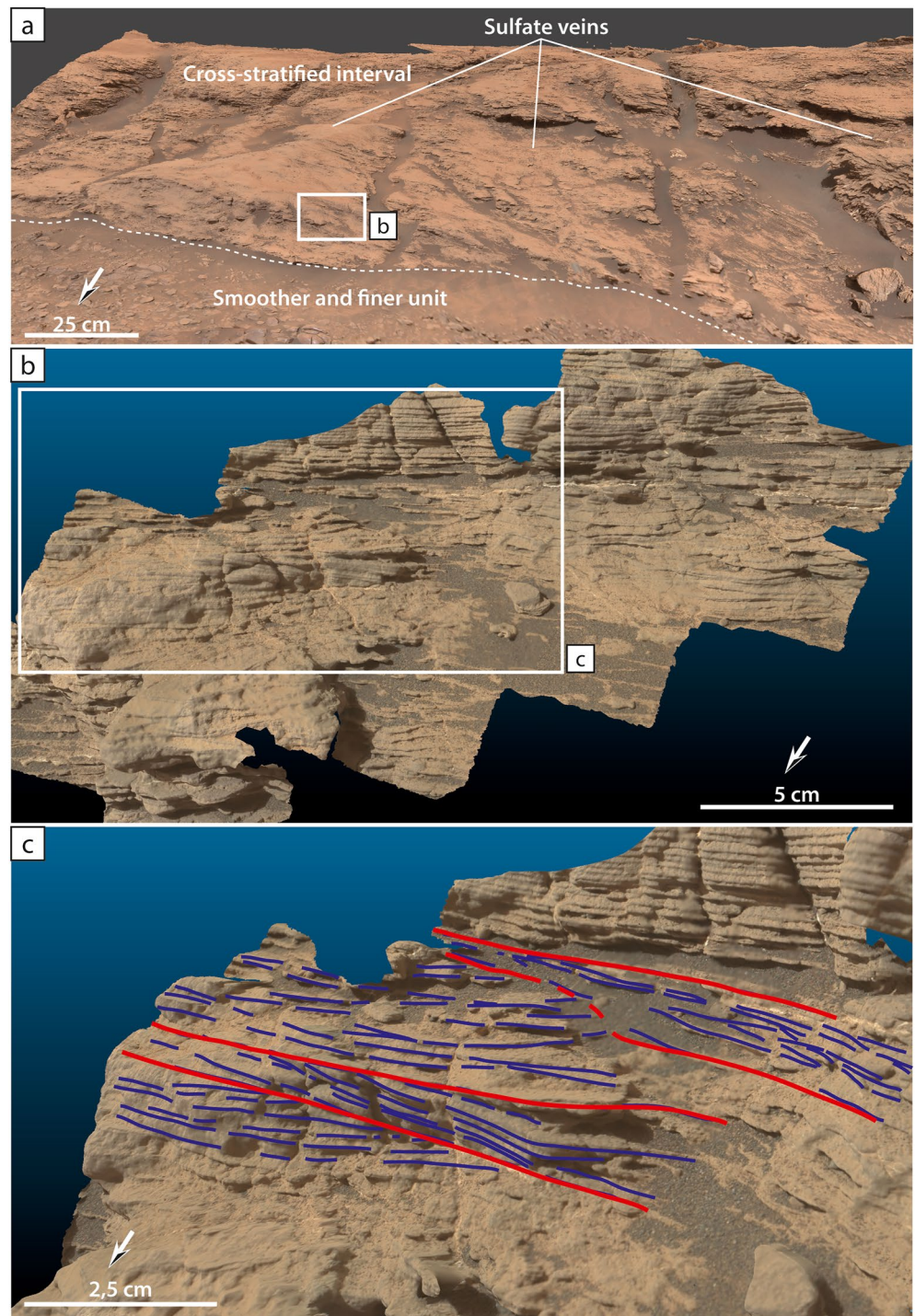


Figure 6. (a) A detailed view of the eastern part of the Teal ridge outcrop on the Digital Outcrop Model (DOM). The dashed line indicates the position of the inferred sharp contact between the mudstone bedrock and the cross-stratified sandstones that compose the mesa. (b) A view of the micro-DOM of the Stack_of_Glencoul target, computed from 15 Mars Hand Lens Imager images taken on Sol 2444; mesh visible on Sketchfab at: <https://skfb.ly/6SE7z>. (c) A detailed view of the micro-DOM showing several bedsets of cm-scale cross-strata with varying direction of apparent sediment transport (blue lines) separated by sharp truncation surfaces (red lines).

The DOM shows that most strata outcropping at Teal ridge are gently dipping southward regardless of cross-stratification. Strata in the center of the outcrop (Figures 5a–5c) seem to “bend” or “roll-over” without significant change of cross-stratification, suggesting a syn- to post-depositional deformation of the structure. The cross-stratification observed at Teal ridge highlights a direction of transport mainly oriented along a SW-NE apparent axis, with a preferential direction toward the SW (e.g., cross-stratification in Figure 5d). However, the concave-based channel-shapes (Figure 5b), a higher order architectural element, are oriented NW-SE, suggesting that channel-scale transport occurred along a NW-SE axis. On Earth, preferential transport direction being perpendicular to the overall direction of the channels is reminiscent of the formation of point bars.

Collectively, these elements point at a depositional setting within a higher energy setting. The coarse-grained cross-stratified sandstones were probably deposited within meter-scale channelized bodies carved in the local finer-grained bedrock. This and the presence of dm- to meter-scale compound cross-stratifications highlights sustained flow at the time of deposition.

4.4. Harlaw Rise

During the southward traverse of the Visionarium area, *Curiosity* stopped at the Harlaw rise locality from Sol 2459 to 2463. *Curiosity* observed several dm- to meter-scale blocks made of laminated and erosion-resistant sandstones. One of these (Figure 7a), consisting of fine- to medium- sandstones, shows a conspicuous pattern of undulating laminations throughout most of its thickness. Several light-toned veins occur either conformable to or cross-cutting the laminations (Figures 7a and 7b).

To better observe the sedimentary features of this block, a micro-DOM has been computed on the MAHLI target Strathdon (Sol 2462; Figure 7b). This model presents two different parts with specific characters, highlighted by differential erosion of the outcrop (Figure 7b). The upper part shows sub-cm-scale undulating laminations, highlighted by differential erosion of the outcrop (green lines on Figure 7c), and the lower part, a recessive bed with faint planar laminae (Figure 7c) whose thickness (when visible) has been measured to be $\sim 0.34 \pm 0.09$ mm. Whereas the undulations in the upper part could be due to soft sediment deformation, the fact that the undulations do not propagate into the lower layer suggests that they may actually represent climbing ripple lamination, a sedimentary feature associated with rapid sedimentation from sediment-rich currents (Allen, 1982). These laminations show a mean lamination thickness of $\sim 0.62 \pm 0.15$ mm. Finally, cross-stratifications observed on the Strathdon target (Figures 7b and 7c) indicate transport along a roughly SW-NE apparent axis.

Collectively, these elements point at two different settings recorded at Harlaw rise. On the one hand, the fine massive mudstones represent a (very) low energy setting; on the other hand, the undulated, cross-stratified sandstones evidence a high energy unidirectional flow. Also, the sharp contact between both finer- and coarser-grained beds indicate fluctuating energy levels.

4.5. Antonine Wall

The Antonine Wall outcrop is situated at the southern end of the Visionarium area and was traversed between Sols 2476 and 2555. The observations there were made in two phases; first from the North and observation of the cliff-face, and later a climb to the top of the mesa to the Glen Etive drill site. Antonine Wall is one of the biggest mesas of the entire Visionarium area, extending about 20 m in continuous cliff-face exposure, and a height of up to 2 m (Figure 8a). It resembles Teal ridge, with a prominent cliff-face that shows mostly fine- to medium-grained sandstones with compound cross-stratification (Figure 8a). In the westernmost part of the outcrop, several dm-thick cross-stratified beds also show a concave base, suggestive of possible channel-shapes, in a similar fashion to that of Teal ridge (cf., Figure S2 in Supporting Information S1). The mesa is elevated above smooth weathering mudstones that surround this exposure. A sharp contact between those two lithologies is inferred at the base of the mesa (dashed line in Figures 8a and 8b).

For a closer inspection of this mesa, a DOM of the Antonine Wall outcrop has been computed (Figure 8b). On this model, we observe cm- to dm-scale cross-stratification in the cliff-face sandstones (Figure 8c). Compared to Teal ridge, cross-stratification is generally smaller scale and shows more variability of sedimentary transport direction (Figure 8c, green lines toward the East, and blue line toward the West). Cross-stratification also appears

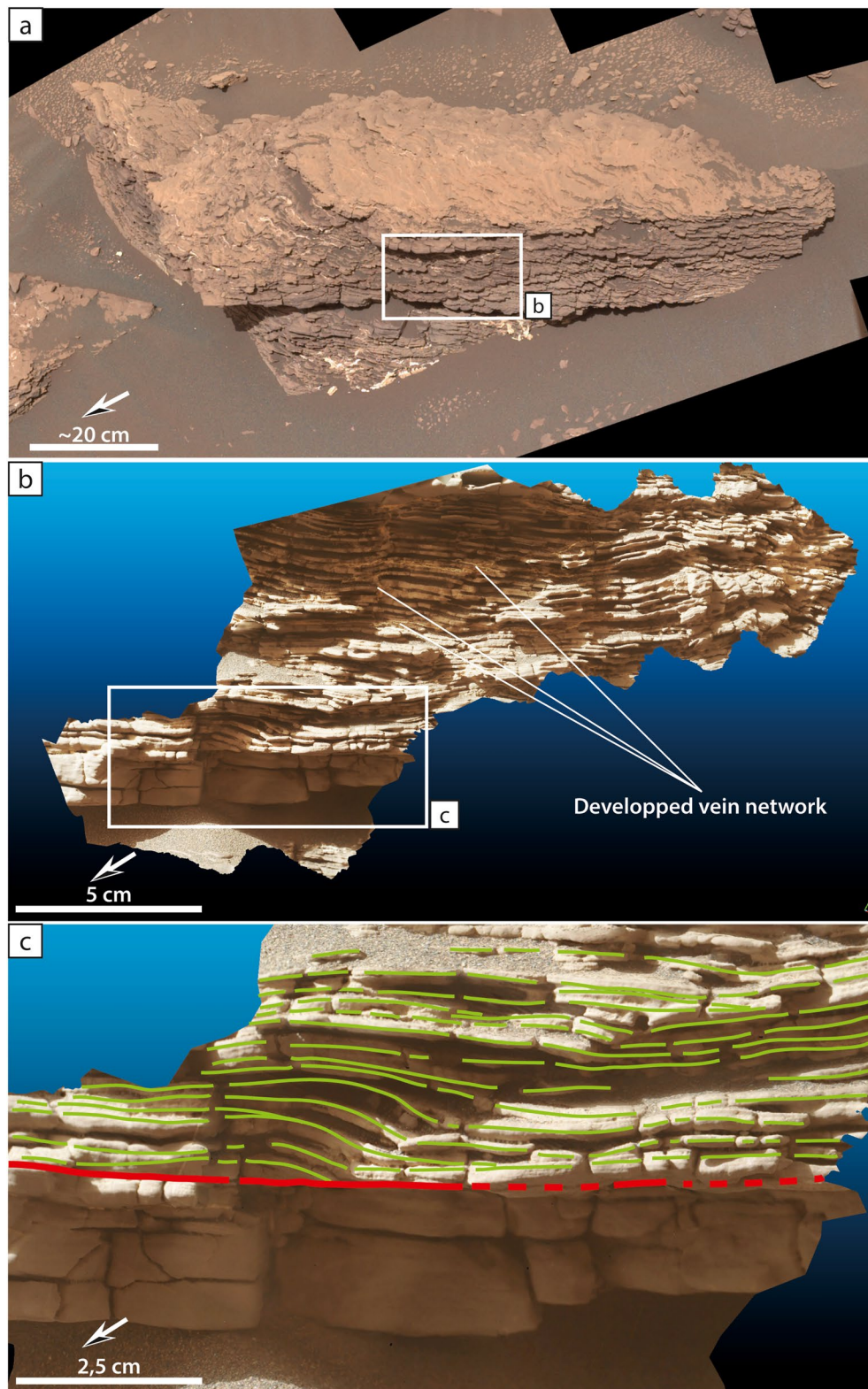


Figure 7.

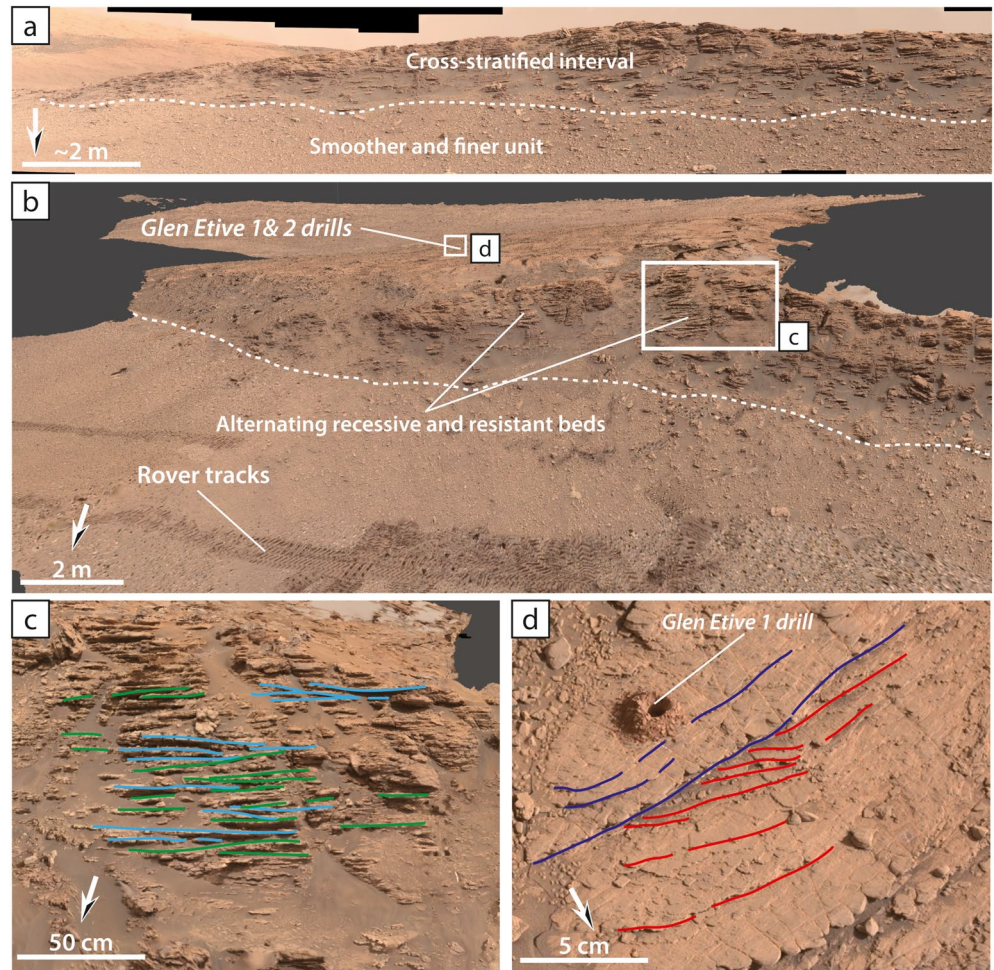


Figure 8. (a) A general view of Antonine Wall outcrop in the Visionarium. Mastcam mosaic acquired on Sol 2471 (sequence mcam013112). The mosaic shows a continuous exposure of cross-stratified sandstones. The dashed line evidences a probable sharp contact of the sandstones over material smoother and finer than sand-sized grains. (b) A general view of the Digital Outcrop Model (DOM) of the locality showing the mesa structure of the ~15 m long outcrop. The sharp contact between smooth fine-grained material and the overlying coarser-cross-stratified interval (dashed line) is clearly visible. Rover tracks have a width of about 40 cm. The DOM was computed from 593 Navcam and 1197 Mastcam images taken between Sols 2471 and 2553; mesh visible on Sketchfab at: <https://skfb.ly/6Z7VL>. (c) A detailed view of the central part of Antonine Wall cliff-face, showing cross-stratification with varying directions of apparent sedimentary transport (green lines toward the East, and blue line toward the West). (d) A close view on the Glen Etive 1 drill site on top of the outcrop that shows an expression of cross-stratification in plan view. Mastcam image 2490ML0132270010904925C00_DRCL.

in planar view at the top of the mesa, for example, around the Glen Etive drill site (Figure 8d). There, several sets of mm- to cm-scale cross-lamination are clearly visible.

This exposure also highlights the resistance to erosion of these cross-stratified sandstones, compared to the mudstone bedrock which decomposes into a multitude of clasts. However, the sandstones seem much more fractured at Glen Etive than at any other outcrop of the Visionarium area (Figures 8b and 8c). Veins are also present on this outcrop within the cross-bedded sandstones interval and can be observed in-between and/or cross-cutting the stratification. The DOM also allows us to observe that most strata of the outcrop are dipping southward, simi-

Figure 7. (a) A general view of a metric-scale block outcropping at the Harlaw rise locality in the Visionarium. Mastcam mosaic acquired on Sol 2461 (sequence mcam013066). The mosaic shows a prominent erosion-resistant meter-scale block cropping out of smoother material. (b) A view of the micro-Digital Outcrop Model (DOM) of the Strathdon target, computed from 18 Mars Hand Lens Imager images taken on Sol 2462; mesh visible on Sketchfab at: <https://skfb.ly/6UEwZ>. A developed vein network is present, with veins in-between and cutting through the laminations. (c) A detailed view of the micro-DOM highlighting a sharp (possibly erosive, red line) contact between a lower (faintly laminated) fine-grained and recessive bed and an upper coarser-grained interval of erosion-resistant undulating and cross-stratified (green lines, climbing ripples) sandstones.

Table 1
Sedimentary Facies Observed in Northern Glen Torridon Region

| Facies | Grain size | Micro-structures | Macro-structures | Post-depositional features | Dynamism | Depositional setting |
|--------|---|--|---|-------------------------------------|---|--|
| A A1 | Mudstones | Massive to sub-mm-scale planar laminations | N/A | Polygonal cracks locally | Very low to low energy | Quiet lacustrine environment |
| A2 | Mudstones and siltstones (locally up to very fine sandstones) | Fine (sub-)mm-scale planar laminations | Mm-scale planar parallel if present | | Low (+) to moderate energy | Shallow lacustrine to lake shore environment, with local current or wave influence |
| B B1 | Very fine and fine (up to medium) sandstones | Mm- to cm-scale cross-stratified (locally undulated) laminations | Dm- to meter-scale crossbedding | Developed light-toned vein networks | Moderate energy in a sustained flow | Distal fluvial environment to shallow fluvially influenced lake margin |
| B2 | Fine-medium (locally up to coarse) sandstones | Cm-scale cross-stratified laminations | Dm- to meter-scale crossbedding and metric-scale channelized bodies | Developed light-toned vein networks | Moderate to high energy in a sustained flow | Dynamic fluvial plain (divagating river channels) |

larly to Teal ridge's. This suggests that the overall transport (and channel orientation) is to the south, and that the observed cross stratification (Figure 8c) reflects 3D bedforms that migrated within these channels.

Collectively, these elements point at a depositional setting similar to that of Teal ridge, albeit being slightly less energetic as hinted by the presence of smaller scale (cm- to dm-scale) cross-strata. Here too, the coarse-grained cross-stratified and mesa-forming sandstones are likely to have been deposited within meter-scale channelized bodies carved in the local finer-grained bedrock. This and the presence of dm- to meter-scale compound cross-stratifications highlight sustained flow at the time of deposition.

5. Interpretation of the Texture and Facies

5.1. Facies and Depositional Settings

Differentiation of facies and sub-facies is based on grain size, multi-scale sedimentary structures and bedforms, and post-depositional features. We defined two distinct facies, each facies being subdivided into two sub-facies that are detailed in Table 1 and illustrated in Figure 9. These facies represent two different depositional settings and were consistently encountered throughout the studied area, in both the Jura and the Knockfarril Hill members.

5.1.1. Facies A: Massive to Finely Laminated Rubbly Mudstones/Siltstones

Facies A is primarily characterized by its fine-grained texture, usually mudstones and siltstones locally up to very fine-grained sandstone (Table 1, Figures 9a and 9b). Most of the exposures of facies A show massive to faintly laminated cm-scale beds (Figure 9a) which characterize the sub-facies A1, whereas sub-facies A2 can locally show mm-scale planar stratification (Table 1, Figure 9c). When laminations are visible, we observe a lamina thickness of 0.35 ± 0.07 mm (Table S2).

Facies A, and more particularly sub-facies A1 is often associated with the smooth and fine-grained bedrock that is mostly encountered in the central and northern parts of the studied area, and within the few massive recessive intercalated beds present at Strathdon or at Glen Etive, in-between more resistant and coarser-grained sandstones of facies B. In some places, such as at Woodland Bay, the sub-facies A1 exposures show the presence of polygonal cracks linked to present-day weathering (e.g., Figure 9a, see Section 5.3). Overall, facies A rocks are not very resistant to erosion, and in most places are recessive relative to sandy lithologies (Figure 7c) or form a cover of cm-scale rubbly pieces of bedrock (cf., Figures 3a, 4b and 9b). Due to its mostly featureless character and the presence of only faint, planar mm-scale laminations, sub-facies A1 is considered to record low energy deposition.

Sub-facies A2 shows an overall similar appearance to sub-facies A1, characterized by fine-grained mudstones and siltstones. The grain size is observed to coarsen locally up to very fine-grained sandstones (e.g., Figure 3c). Sub-facies A2 also features mm-scale planar parallel lamination (cf., Figures 3b, 3c and 9c) with the local pres-

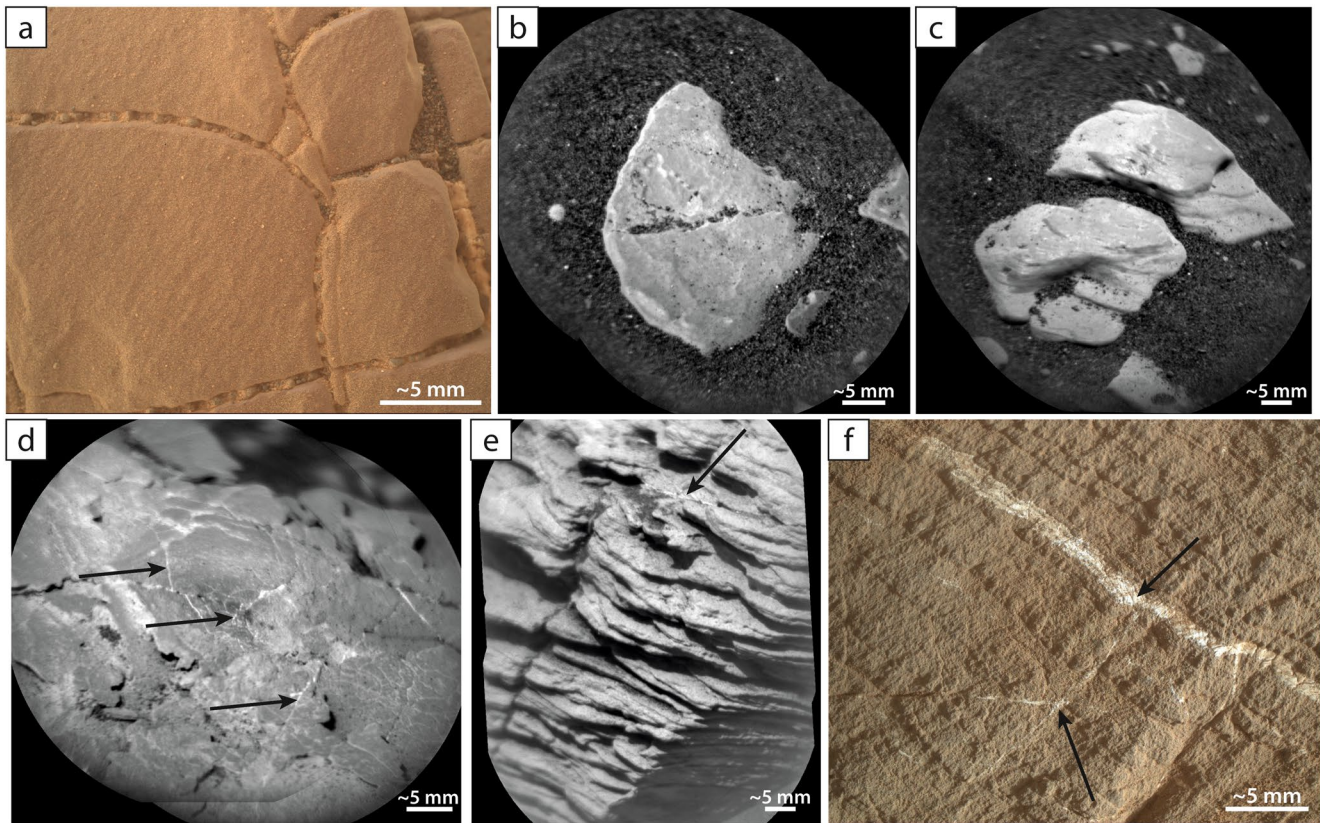


Figure 9. Sedimentary facies observed across the Jura/KHm boundary; Arrows point to calcium sulfate veins. (a) Facies A1, smooth and rubbly massive mudstone, locally exhibiting cracks. Mars Hand Lens Imager (MAHLI) image of target “Crakaig” acquired on sol 2422 (2422MH0007150010900895C00). (b) Facies A1, smooth rubbly mudstone without crack. ChemCam RMI image of target “Hillhead_ccam” acquired on sol 2419 (ChemCam sequence ccam01419). (c) Facies A2, smooth and rubbly mudstone/siltstone, exhibiting fine (sub-)mm-scale planar laminae. ChemCam RMI image of target “aegis_post_2418a” acquired on sol 2418 (ChemCam sequence ccam05416). (d) Facies B1, erosion-resistant cross-stratified fine to medium sandstone. ChemCam RMI image of target “Feshie_ccam” acquired on sol 2461 (ChemCam sequence ccam02461) with LIBS raster hitting a sulfate vein. (e) Facies B2, coarser erosion-resistant cross-stratified medium (to coarse) sandstone. ChemCam RMI image of target “Yesnaby_Stacks” acquired on sol 2444 (ChemCam sequence ccam01444). (f) Facies B2, laminated medium sandstone. MAHLI image of target “Beauly” acquired on sol 2443 (2443MH0007230010901502C00).

ence of low-angle truncation surfaces and current produced lamination, suggesting that in places at least facies A was deposited in shallow water with frequent current or wave activity.

Facies A is therefore interpreted as representing deposition in a lacustrine environment that was in places shallow enough to preserve a record of current and possibly wave reworking.

5.1.2. Facies B: Cross-Stratified Fine to Medium Sandstones With Light-Toned Veins

Facies B is primarily characterized by its coarser-grained texture, from fine (Table 1, Figure 9d) to medium-grained sandstone, locally up to coarse-grained sandstone (Table 1, Figures 9e and 9f). This coarser facies is also characterized by the presence of compound cross-stratification, with bedset thickness ranging from mm-scale to dm scale and even m-scale (Table 1, Figures 5d, 6c and 8c). Lamination thickness in facies B is typically between 0.5 and 1 mm (Figures 9e and 9f, Table S2), but can be up to cm-scale locally. Sub-facies B1 and B2 are mainly differentiated by their grain size, with B2 showing a larger proportion of medium, locally up to coarse, sand grains with cm-scale cross-stratification (Table 1). Most exposures of facies B are in the form of dm- to meter-scale blocks or slabs that protrude from the finer grained and rubbly bedrock in the northern part of GT (e.g., Kilmalie/Aberlady drill site and Harlaw rise, Figures 4 and 7). Facies B is also the predominant facies in the meter-scale mesas observed in the Visionarium (e.g., Teal ridge and Antonine Wall outcrops, Figures 5, 6 and 8). It becomes the dominant observed facies from Teal ridge southwards (cf., Figure 1c). This facies is also characterized by the presence of well-developed light-toned vein networks (Figures 4d, 6 and 7b and arrows in Figures 9d–9e). Some of these veins have been hit by ChemCam’s LIBS, as seen in Figure 9d. Facies B rocks are overall resistant to

erosion, as observed through their consistent exposures as mesas or individual blocks and slabs cropping out of the finer bedrock. In some places, the coarser sandstones are also fractured, such as at Antonine Wall (Figure 8b).

The compound cross-stratifications observed in facies B sandstones (e.g., Figure 5) suggest sustained flow over extended time periods (Allen, 1982), plausibly associated with fluvial processes (channels and sandy braids) or a fluvially influenced lake margin setting (distal deltaic distributaries). Comparable cross-stratification has been observed elsewhere in the Murray formation (Schieber, Bish, et al., 2017; Schieber, Stein, et al., 2017; Stack et al., 2019) but does not appear to occur in the same depositional context.

At GT, the observation of compound cross-stratification in likely channel-fill sandstone bodies (Figures 5b and 5c and Figure S2 in Supporting Information S1) argues against deposition by short-lived flow events. Instead, bedform organization at the observed scale implies relatively steady uniform (and unidirectional) flow of at least many hours duration (Bohacs, 1981), an interpretation that is consistent with sustained flow in fluvial channels. The variable orientation of cross-beds seen in facies B outcrops (e.g., Teal ridge, Harlaw rise, and Antonine Wall) is also consistent with migration of 3D bedforms (dunes or braids) through fluvial channels. A general southward dip of facies B strata and SE-NW oriented channel forms also argue for the former presence of a well-developed and temporally continuous fluvial system.

Sub-facies B1 may represent deposition under moderate energetic conditions that can be observed in both a distal fluvial system or within a fluvially influenced proximal shallow lake margin. Sub-facies B2 probably represents more energetic conditions encountered in fluvial channels or deltaic distributaries. These observations and deductions suggest that the irregularly distributed resistant outcrops and mesas seen throughout the Visionarium are remnants of fluvial channels.

5.2. Geometric Relations Between Facies A and B

In the studied area, facies A and B denote differing environmental and energetic conditions that are encountered in close lateral proximity without any conspicuous unconformity separating them (e.g., at Kilmorie/Aberlady drill site), and even appear interstratified in places (e.g., at Woodland Bay or at Antonine Wall). It is common to observe sandstone bodies with affinity to facies B within areas dominated by facies A, as well as occurrences of facies A type lithologies within larger bodies of facies B.

We observe two types of stratigraphic relationships between facies A and B throughout the northern GT area and within the Visionarium. First, a progressive transition can be documented (left on Figure 10) showing dm- to meter-scale alternations and interfingering between both facies. This progressive transition is evidenced within alternating fine- and coarser-grained beds at Woodland Bay (Figure 3). A similar relationship is also seen in some intervals of the Antonine Wall outcrop with occurrences of recessive finer-grained layer alternating with resistant and cross-stratified sandstones (Figure 8c). This alternating/interfingering architecture is observed in GT area and was called “Flodigarry facies,” notably at Woodland Bay (e.g., Bristow et al., 2021; Edgar et al., 2020; Fedo et al., 2022; Rudolph et al., 2020). We propose that the “Flodigarry” outcrop is not a “facies” per se but rather reflects the progressive transition between facies A and B. Second, a sharp (possibly erosive) meter-scale discontinuity between facies A and B is observed in places (Figure 10), most particularly at the base of Teal ridge and Antonine Wall mesas (Figures 6 and 8). There, coarse-grained cross-stratified deposits belonging to facies B are seen deposited above facies A fine-grained deposits. Some intermediate stages can be observed at a smaller scale, for example, at Harlaw rise (Figure 7) where a sharp truncation occurs at the base of the facies B interval that overlies finer-grained and recessive facies A bed.

The presence of these two types of spatially distributed transitions between the same two facies suggests differing levels of depositional and erosive energy across the area. First, we observe facies interfingering in the northern part of the study area (cf., Figures 1 and 10) which also represents the lowest elevations in the GT area (at approximately $-4,154$ m). In that case the transition involves facies A and B1, representing a presumed low to moderate energy (shore) lacustrine environment, and moderate but sustained energy settings related to a fluvial influence on the lake-margin, respectively, probably reflecting shoreline regression as the lake margin was infilled with sediment. Upsection and farther South, these gradual transitions are “replaced” with channel sand bodies that appear to fill erosive incisions into the underlying lacustrine mudstones (cf., Figures 1 and 10). These erosive contact relationships suggest deposition on a fluvial plain with channel incision forced by either high flow events or lowering of lake level. Assuming a prevalence of southward sediment transport, the upward progression from facies A to dominant facies B with channel incisions can be

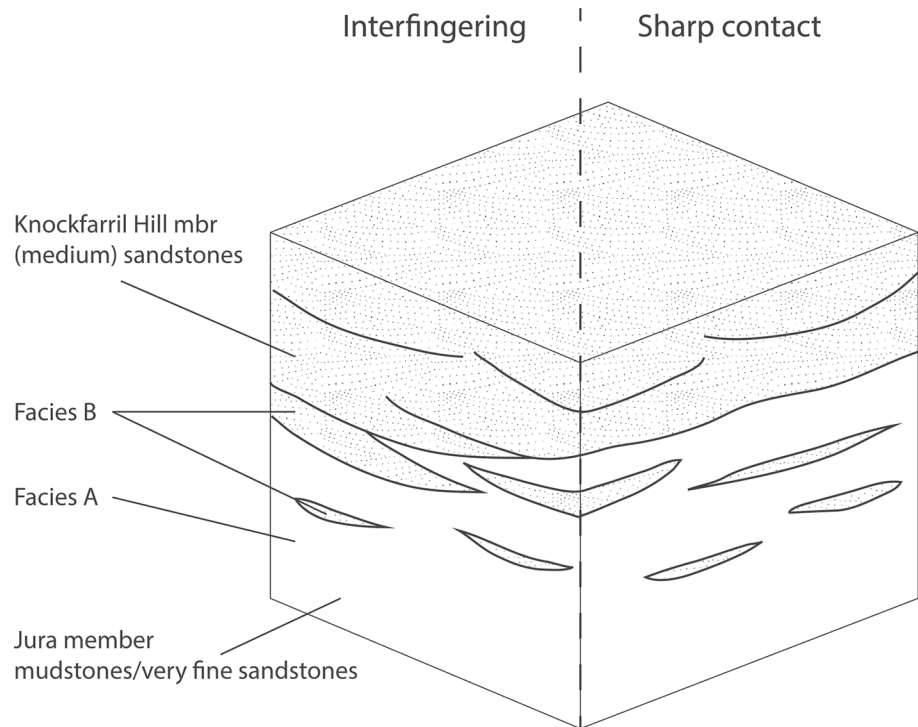


Figure 10. Schematic representation of the two types of geometric relations observed at the outcrop between facies A and facies B. Left: progressive transition marked by the presence of alternating/interfingering beds of both facies (e.g., Woodland Bay). Right: Sharp, likely erosive and laterally continuous contact between facies A and B, with B replacing A (e.g., mesas of Teal ridge and Antonine Wall).

considered a plausible outcome of southward sediment transport that first filled up (exhausted) accommodation along the lake margin, and thus, over time, pushed the shoreline and lake margin fluvial plains further south.

5.3. The Origin of Polygonal Cracks at Woodland Bay

The Woodland Bay outcrop (Figure 1c) contains polygonal crack patterns in multiple resistant sediment layers that have not been observed elsewhere in the studied area (Figures 3a and 11a). These cm-scale cracks are present on several low-relief exposures rising from the regolith and surrounding rubble as dm- to meter-scale patches, most likely representing the same bedding plane (Figure 11a).

The observed polygonal-cracked layers are interstratified with softer thinly layered intervals, parting planes are well developed, and in side view the cracks are parallel-sided and may terminate upon encountering the softer intervals. In contrast, desiccation cracks would be expected to taper downwards. In outcrop, the cracked layers tend to “peel off” from the underlying softer strata. These observations suggest mechanical decoupling between polygon layers and soft interbeds. Although these cracks resemble geometrically those at “Old Soaker” (lower in the section; Schieber, Bish, et al., 2017; Schieber, Stein, et al., 2017; Stein et al., 2018), polygonal geometries such as these form whenever a coherent layer undergoes shrinkage, no matter what the underlying cause (Chan et al., 2008; Cosgrove & Hudson, 2016; Loope & Burberry, 2018; Williams & Robinson, 1989). The observation that we see both rectilinear and hexagonal fracture patterns on the same surface (Figure 11b) suggests that the formation of the observed crack patterns involved many opening (contraction) cycles (Goehring, 2013). The grain size of polygon layers observed with MAHLI (Figure 11c, Figure S3 in Supporting Information S1) suggests that they likely are coarse mudstones (aka siltstones). Because of framework grain support, siltstones do not contract upon drying and thus are unlikely to form desiccation cracks. Also, had these cracks formed at the time of sediment deposition, one should expect to see evidence of lithified crack fills (e.g., Stein et al., 2018). The

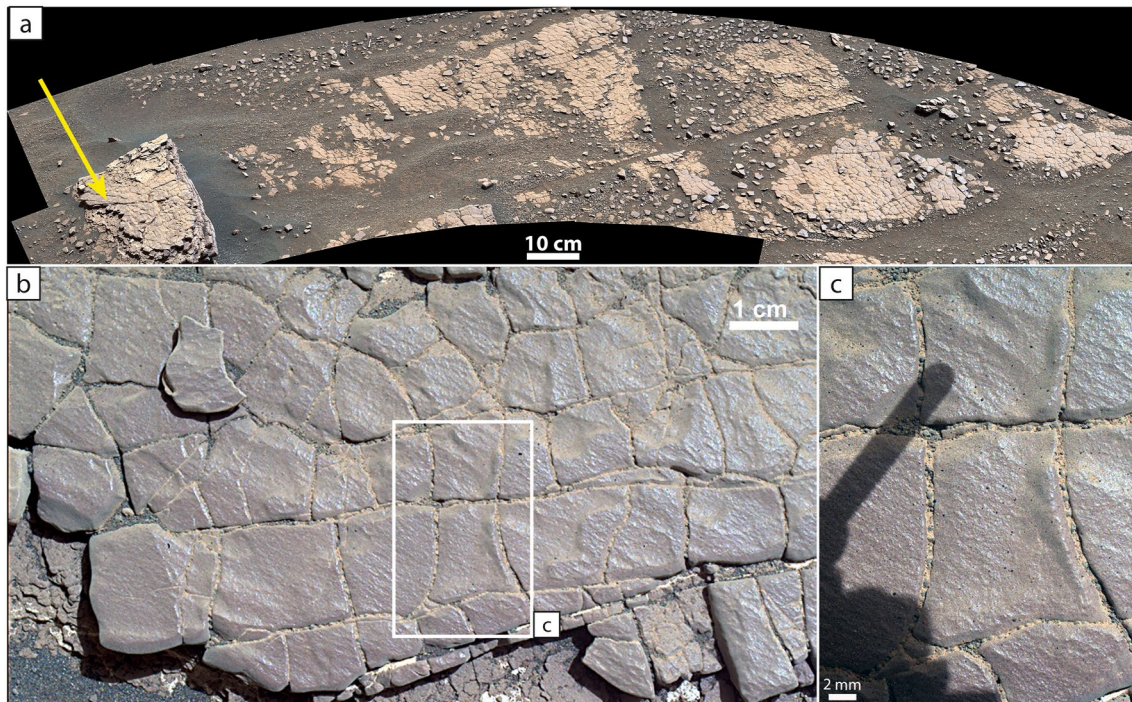


Figure 11. (a) A general view of the Woodland Bay outcrop toward the polygonal-cracked patches. Mastcam mosaic acquired on Sol 2424 (sequence mcam012841). With the exception of the far left block (yellow arrow), these may represent a single bedding plane. (b) A detailed view of the target Crakaig yellow arrow on (a) showing well-developed polygonal crack patterns (Mars Hand Lens Imager image 2422MH0007060010900870C00 acquired on Sol 2422). (c) A closer detailed view showing that the cracks are filled with modern surface sediment, aeolian sand, silt, and dust, with no indication of a lithified crack fill.

absence of such fill lends further credence to a weathering related origin of these cracks because we only observe modern-day, wind-blow sediment filling those cracks (Figure 11c).

Collectively, the observations made on the Woodland Bay polygonal-cracked layers are consistent with and of the same scale and characteristics as polygonal networks observed during outcrop weathering of mudstones on Earth, and likely caused by thermal cycling. Given the large day-night temperature differences on Mars, thermal expansion-contraction of surface layers is a plausible process for the formation of the polygonal-cracked layers, and the cracks are most likely unrelated to the original depositional environment of these strata.

6. Geochemical Compositions and Trends

6.1. Major Oxide Composition

Here, we investigate the Major Oxide Composition measured by the ChemCam instrument on our subset of 36 targets within or near the main outcrops described above (detailed list in Table S1, complete data in Table S3). We want to test the existence of a possible relationship between the sedimentary facies A and B described above and the geochemical variability observed in GT. To that purpose, we focus on oxides SiO_2 , CaO , MgO , Na_2O , and K_2O . Other compositional trends observed within bedrock geochemistry (e.g., TiO_2 , Al_2O_3 , and FeO) and their in-depth analyses are beyond the scope of this study and are addressed in detail in the companion work by Dehouck et al. (2022). To test the existence of a possible relationship between the sedimentary and geochemical characters, individual points of measurements are colored in Figure 12 according to the facies determined for each corresponding target (Table S3).

Figure 12 shows the abundances for CaO , MgO , K_2O , and SiO_2 . Most of the CaO values (including all facies A samples) are concentrated in an area of the plot close to GT mean values (indicated by the whiskers on Figure 12a, <2 wt.%). Facies B targets show higher CaO values (>2 wt.%), especially for those belonging to sub-facies B2 (>2 wt.% and up to ~ 8 wt.%). This enrichment is likely related to the light-toned veins frequently observed in targets of this sub-facies (e.g., Figures 10d and 10f), which are composed of calcium sulfate, as previously

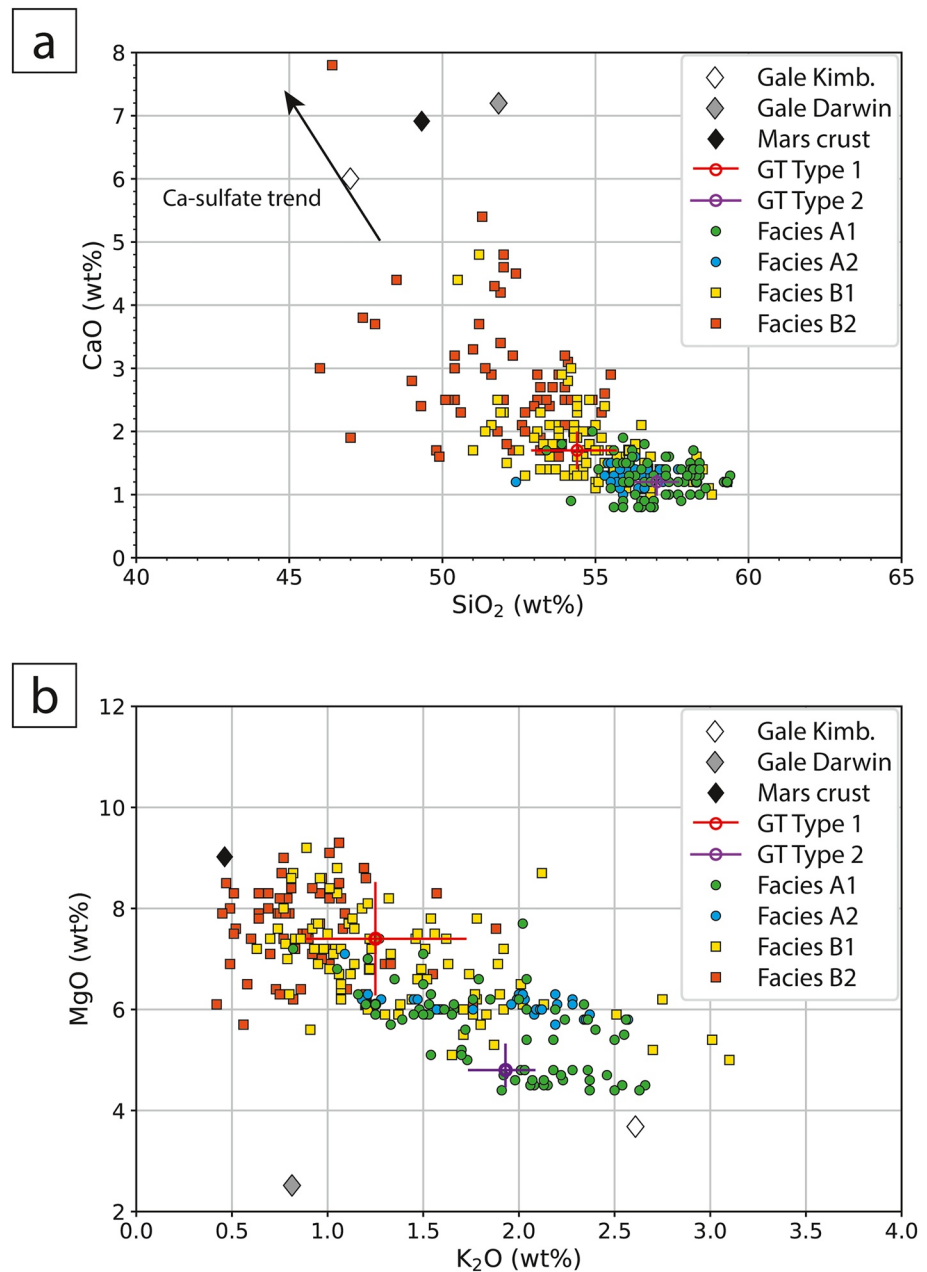


Figure 12. Major-oxide compositions of representative GT targets in CaO, SiO₂, MgO, and K₂O (in wt.%). Each dot represents a single analysis point, colored as a function of its sedimentary (sub-)facies A1, A2, B1, and B2. Types 1 and 2 are the “coherent” and “rubby” endmembers described by Dehouck et al. (2022). (a) CaO versus SiO₂ plot. Arrow represents the trend to Ca-sulfate compositions. (b) MgO versus K₂O plot. Average Martian crust values from Taylor and McLennan (2009); average Gale basin conglomerates values from Mangold et al. (2016) (Kimb.: Kimberley).

observed along *Curiosity*'s traverse (e.g., Nachon et al., 2014, 2017; Rapin et al., 2016, 2019). The lower SiO₂ content of the B2 targets (<55 wt.%) is consistent with this interpretation. Overall, facies B shows values closer to the Martian average crust (Taylor & McLennan, 2009) and Gale conglomerates (Mangold et al., 2016, Figure 12a) for the two oxides considered here.

A clear compositional difference between samples from facies A and B is also observed in the MgO versus K₂O plot (Figure 12b). LIBS points identified as facies A show a lower mean MgO content (5.7 ± 0.8 wt.%) and a higher mean K₂O content (1.9 ± 0.4 wt.%). Conversely, LIBS points belonging to facies B show a higher mean

MgO content (7.1 ± 1.0 wt.%), and a lower mean K₂O content (1.3 ± 0.7 wt.%). Here again, facies B shows the closest values to average Martian crust. On the other hand, when comparing to the Gale conglomerates, we observe that facies A1 is closest to the Kimberley conglomerates, a K-rich deposit previously identified on Aeolis Palus (Mangold et al., 2016). Despite the observed difference in K₂O content, facies A and B show similar Na₂O values, close to both the average Martian crust and the Kimberley conglomerates (Figure S4 in Supporting Information S1).

Thus, facies A and B display significant differences in major element abundances that may be a consequence of their distinct texture and depositional mode.

6.2. Relation Between the Studied Facies and Regional Geochemical Endmembers

The GT region shows a geochemical composition of the major elements that is broadly in line with the underlying Murray formation, but with some notable variability (e.g., Dehouck et al., 2021, 2022). In the Jura member, two endmembers have been identified from both the APXS and ChemCam measurements (e.g., Dehouck et al., 2022, 2021; O'Connell-Cooper et al., 2022). These two endmembers were referred to as “rubbly” and “coherent” from the relative resistance to erosion of the corresponding rocks (Dehouck et al., 2022), with the “rubbly” consistently outcropping as small pieces of fragmented bedrock (e.g., Figure 9a), whereas the “coherent” is represented by larger blocks and slabs (as observed at e.g., Kilmalie/Aberlady and Teal ridge).

These two endmembers are mainly discriminated based on their MgO and K₂O contents (Dehouck et al., 2021, 2022; O'Connell-Cooper et al., 2022). The “rubbly” endmember shows a K₂O-rich (>1.5 wt.%) and MgO-poor (usually <6 wt.%) composition, defined as the regional Type 2 composition by Dehouck et al. (2022). The “coherent” endmember shows higher MgO content (~6–11 wt.%) and a lower K₂O content (<1.5 wt.%) defined as the regional Type 1 composition by Dehouck et al. (2022).

Figure 12b is thus most important in seeking a potential relation between the geomorphic expression at the outcrop, sedimentary facies, and geochemical signals in GT. We observe a clear distinction between facies A and B samples in the Mg and K contents. The fine-grained and rubblier facies A is in line with high-K Type 2; and the coarse-grained, slab-forming facies B is mostly in line with high-Mg/low-K Type 1 compositions. However, the sub-facies B1 shows a more important scattering of the K₂O values than the other sub-facies. This could be the result of a local mixing of sedimentary material at the interface between facies A and B, which is compatible with the alternating and interfingering depositional mechanism that we have highlighted on several outcrops (see Section 5.2).

Overall, targets from facies B have a composition closer to the average Martian crust compared to targets from facies A (Figure 12). This difference could reflect a less pronounced aqueous alteration of facies B material. However, the values of the Chemical Index of Alteration are similar for the Types 1 and 2 endmembers (Dehouck et al., 2022). Alternatively, the difference in composition could be due to a difference in sediment provenance, with facies A material being derived from a more K-rich source. The existence of a K-rich source in the Gale watershed was already inferred earlier in the mission based on the observation of potassic sandstones and conglomerates at the Kimberley location (Le Deit et al., 2016; Mangold et al., 2016; Treiman et al., 2016).

7. Discussion

7.1. Significance of the Facies and Stratigraphic Evolution From Jura Member to Knockfarril Hill Member

As we elucidate the stratigraphic and paleoenvironmental evolution of the studied area and broader regional context, it is important to recognize the relations between the facies characterized in this work and the members of the Murray and Carolyn Shoemaker formations defined by the MSL team. These members are defined by the team from both the characters as seen from orbital (spectro-) images, and the textures deciphered using in situ observations made using *Curiosity*. Yet, from their sedimentary characters (textures, laminae thicknesses, and structures) and their overall spatial distribution, both facies A and B fall in line with previously described members present in the GT area: the Jura and Knockfarril Hill members, respectively (e.g., Bennett et al., 2022; Edgar et al., 2020; Fedo et al., 2020, 2022). However, from a textural and sedimentary point of view, the Jura/KHm boundary (Figure 13a) has been drawn from orbital and in situ observations based on the difference in

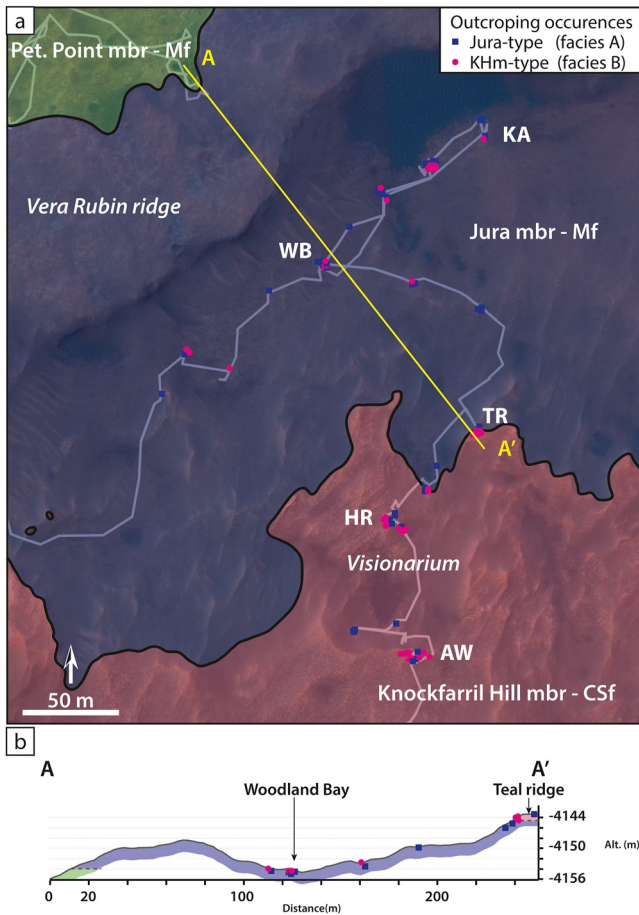


Figure 13. (a) Spatial distribution of the studied target, along the traverse after their characterized sedimentary Jura- or KHm-type facies. This map shows that both facies are observed occurring within both members mapped area, demonstrating a progressive transition between them rather than a sharp geographic boundary. Regional geological basemap after Fedo et al. (2022). WB: Woodland Bay, KA: Kilmarie/Aberlady drill sites, TR: Teal Ridge, HR: Harlaw rise, and AW: Antonine Wall and Glen Etive drill site; Mf: Murray formation and CSf: Carolyn Shoemaker formation (cf., Figure 2). (b) Regional cross section of the northern GT area from Vera Rubin ridge and down to the Visionarium area.

resistance to erosion, an approach that does not capture the smaller-scale local variability in facies. Thus, observed occurrences of facies A can be referred to as “Jura-type deposits” whereas facies B beds can be referred to as “KHm-type deposits” to avoid any ambiguity with the mapped units.

We have shown above that the chemical composition of the bedrock varies between two regionally observed endmembers that are consistent with sedimentary defined Jura-type and KHm-type deposits, implying a link between the facies and the geochemical signal. Specifically, on the one hand, the Type 2 endmember (as defined by Dehouck et al., 2022) is associated to rubbly outcrop expressions and morphologies, therefore corresponding to fine-grained Jura member facies. On the other hand, the Type 1 endmember corresponds to coherent and slab/ridge-forming morphologies, therefore associated with coarser-grained KHm facies.

Outcrops with a Jura-type signature within the mapped KHm member can be interpreted as occurrences of Jura member material within the coarse-grained KHm member, and vice versa, where KHm-type signatures within the mapped Jura member can be interpreted as occurrences of KH member. Consequently, the two samples acquired within the mapped Jura member during the GT campaign (Aberlady and Kilmarie) have sedimentological and geochemical characteristics that link them to KHm-type deposits. The “true” Jura-type material, on the other hand, was too fragmented to be sampled with the drill.

Whereas a clear topographic and textural change is observed between Jura and KHm members in the regional orbital imagery from HiRISE, allowing for mapping those two units at the regional scale (Figure 13a, Bennett et al., 2022; Fedo et al., 2022), this distinction is not as clear and obvious from rover observations along the traverse. Indeed, Figure 13 shows that the spatial distribution of Jura-type and KHm-type material exposures across the region are scattered laterally (Figure 13a) as well as vertically (Figure 13b). The cross section in Figure 13b demonstrates that KHm-type deposits are observed as low as $-4,154$ m in elevation, which is 10 m below the mapped limit of the KHm *sensu stricto*. Conversely, Figure 13a also shows the recurring presence of fine-grained Jura-type deposits within the KHm map area (blue squares in Figure 13), indicating coexistence of energetic fluvial and less energetic lake margin depositional settings. This geographic distribution means that strata typical of the KHm occur somewhat lower, and therefore earlier in the history of GT than suggested by the regional mapping. It also indicates a more complex history, with laterally and vertically alternating deposition of Jura-type and KHm-type materials during the time interval represented by the ~ 10 m-thick succession observed in the study area.

In summary, the fine-grained facies of Jura member represents quieter settings dominated by lacustrine processes, whereas coarser-grained and cross-stratified facies of KHm represents more energetic, fluvially influenced lake margin and fluvial channel settings. The spatial distribution of both facies, their gradual as well as sharp contact relationships, together with their specific geochemical signature (Types 2 and 1 endmembers, respectively), collectively are the expression of a dynamic depositional setting and lateral facies migration. The widespread dominance of fluvial deposition at the onset of the KHm *sensu stricto* (as mapped) may reflect accelerated southward facies migration due to increased sediment supply or a forced regression of the lake shoreline due to either a lake level drop and/or a change of localization of the regional depocenter.

7.2. A Progressive But Marked Change in the Regional Depositional Settings in Glen Torridon Across the Jura/Knockfarril Hill Members Boundary

Up to the VRR, *Curiosity* has been exploring 300+ m of mostly fine-grained lacustrine strata of the Murray formation. Arriving at GT, however, we observe a change in the stratigraphy representing an important shift in the regional depositional setting toward more energetic conditions over a comparatively short time period (~10 m thick interval, likely representing multiples of 1,000s to 10,000s of years). This transition is marked by the onset and increasing occurrence of the KHm-type sandstones, characterized by fluvial processes. We therefore propose that this interval records a significant change in the regional organization of the Gale crater depositional system. This change could have been caused by migration of the lake margin, perhaps due to substantial drop in the regional base level. Such a drop would force basinward migration of the shoreline and favor the observed lateral and vertical shift from lacustrine to fluvial settings in the study area. We can hypothesize that changes in climate could have caused a decrease of water supply, lead to lake level drop and migration of the regional depocenter, and thus a general expansion of fluvial plains. Indeed, the KHm sandstones interval continues up section for more than 10 additional meters (cf., Figure 2; Fedo et al., 2022) indicating that fluvial conditions were sustained for a significant time interval in the area.

This trend toward a subaerial evolution of the basin also has potential to be investigated at a larger scale. As the rover continues to climb up, it will be important to test whether the paleoenvironmental change recorded at the Jura/KHm boundary is restricted to the GT area or if it is a part of a broader evolution of the depositional settings in Gale crater, as hinted at by decameter-scale cross-stratified deposits observed in the overlying so-called “sulfate unit” (corresponding to the Pontours member of Carolyn Shoemaker formation; cf., Figure 2 and Fedo et al. (2022)) that are thought of to be of aeolian origin with local fluvial inputs (Rapin et al., 2021).

7.3. Geochemical Processes Associated With Sedimentation

A lacustrine setting often produces a “homogeneous” geochemical signal because sediments from the various sources and inputs of the basin are mixed; conversely, the composition of a fluvial deposit reflects more directly the composition of the source rocks encountered in the watershed (e.g., Garzanti et al., 2011; Jin et al., 2006; Sawyer, 1986). As we observe variations in the GT paleoenvironmental conditions across the Jura/KHm boundary, the correlation between sedimentary and geochemical parameters is interpreted to reflect this regional change in depositional settings.

We have demonstrated that in GT, a strong relationship exists between the sedimentary and the geochemical records, with each facies displaying a characteristic geochemical signature, which is Si- and K-rich for the Jura-type material on one hand, and Si-poor, K-poor, and Mg-rich for the KHm-type material on the other hand. These variations in abundances could be associated with several processes such as (a) the impact of fluid circulation during cementation and/or diagenesis, (b) a mechanical segregation related to the changing energy of the depositional setting and/or proximity to primary sources, or (c) the influence of the accumulation, and/or (d) in situ formation of clay minerals, which is of particular interest in the GT area, aka the “clay-bearing unit.”

The KHm-type material is characterized by its coarser-grained texture (fine- to medium-grained sandstones) due to deposition under energetic fluvial conditions, and good outcropping conditions as erosion-resistant pluri-dm-scale slabs to pluri-meter-scale mesas (particularly in the Visionarium area). This resistance to erosion can be linked to a higher degree of cementation. The larger grain size of these sandstones is a favoring factor because it implies a primary porosity that increases the potential for fluid circulation and subsequent cementation during burial (e.g., Bjørlykke, 1988; Hiatt & Kyser, 2000). Cementation and fluid circulation are plausible processes for enhanced accumulation of Mg (notably in cements), and for the depletion of K due to destruction of labile minerals (e.g., Argast & Donnelly, 1987; Jin et al., 2006).

The KHm-type material is also characterized by the presence of well-developed light-toned vein networks, that are both observed at the outcrop, and detected through the geochemical signal with higher values of CaO and lower values of SiO₂ in the coarsest targets of the facies B2, which are commonly associated in Gale crater with secondary sulfate vein formation (e.g., Nachon et al., 2017, 2014; Rapin et al., 2016). Those veins are absent from the more massive and fine-grained Jura-type material, highlighting the mechanical contrast between KHm and Jura rocks. The latter, being poorly cemented and mechanically weak, more likely deformed instead of fracturing, whereas the former are likely to have behaved rigidly and prone to fracture formation. Thus, secondary porosity

due to fracture formation, as well as later stage fluid circulation and mineralization should largely be restricted to the sandy KHm rocks.

Mechanical segregation of minerals may be a cause for K-enrichment within finer-grained Jura-type material. This mechanism implies that throughout their transport, minerals can be sorted according to their density, and therefore, K bearing minerals (such as K-feldspar) may have been preferentially transported and deposited under lower energy conditions due to its lower density compared to mafic mineral grains (e.g., Argast & Donnelly, 1987; Jin et al., 2006; Sawyer, 1986). As the Jura-type material is representative of lower energy depositional settings, such a mechanism could explain the observed local enrichment in K. A similar relationship was already observed earlier in the mission by Siebach et al. (2017) with K concentrated in the fine fraction resulting from the alteration of feldspar-rich protolith. This hypothesis of a role of the transport is also supported by comparing both materials' signature with the average Martian crust (Taylor & McLennan, 2009) and the Gale basin average conglomerates (Mangold et al., 2016). We can see that the coarser-grained fraction of the KHm-type material is overall closer to the average crustal composition, indicative of a sediment possibly closer to its primary source. On the contrary, K-rich Jura-type material shows a conspicuously differing composition and systematically more distant from the average crustal values, indicative of a reworked and/or more evolved sediment. This latter's origin might be related to a different sedimentary source, similar to previously identified K-rich bedrock sources within the Gale crater watershed indicated by the K-rich sandstones and conglomerates observed at Kimberley (Le Deit et al., 2016; Mangold et al., 2016). As Jura-type material exhibits K_2O values close to that of the Kimberley conglomerates (Figure 12b), a common origin with Kimberley's sediments cannot be ruled out.

Finally, whereas this hypothesis is compatible with a model in which K is leached from coarser-grained sediments with higher porosity such as from the KHm-type material, an alternative hypothesis, supported by observations on minor elements (Cousin et al., 2021; Dehouck et al., 2022), suggests that enrichment in K could also be due to the presence of illite, a K-rich clay mineral that would have been segregated mechanically during transport from the coarser sediment fraction (KHm). Post-depositional incorporation of potassium in clay minerals (as suggested by Thorpe et al., 2020) is yet another process that needs to be considered.

8. Conclusions

As the *Curiosity* rover entered the GT area, it encountered strata that differed notably from the underlying ~300 m of Murray formation. The sedimentary succession of the area consists of two contemporaneous facies: a mudstone-dominated "facies A" that accumulated in a low-energy lacustrine setting and shows evidence of current reworking in presumed lake margin locations and a sandstone-dominated cross-stratified "facies B" associated with sustained energy, channel fill deposits in alluvial plains and fluvial-influenced lake margin settings. Facies A and B are typical of rocks from the Jura and Knockfarril Hill members, respectively, with significant exceptions as these facies are observed to alternate and/or interfinger with each other across the mapped Jura/KHm boundary. This suggests that these facies coexisted across the area, and through time shifted laterally in response to sediment supply and/or base level changes.

Geochemically, facies A and B can be considered compositional endmembers, corresponding to regionally recognized Types 2 and 1 compositions, respectively (2 being K-rich; 1 being K-poor and Mg-rich). Data points along the traverse reflect the intermingling of facies and the upward shift from facies A to facies B.

The paleoenvironmental shift across the Jura/KHm boundary has been documented through sedimentological analysis of outcrops and is mirrored by the changes in the chemical compositions collected from these same locations. This transition, first progressive as illustrated by the interfingering of the two facies, and then expressed up section as sharper erosive contacts between the two, reflects the onset and then steady expansion of fluvial dominated depositional environments in the study area. The underlying causes for this change could be local or regional drop of base level, possibly in relation with changing global climatic conditions at the Noachian/Hesperian boundary.

Conflict of Interest

The authors declare no conflicts of interest relevant to this study.

Data Availability Statement

All of the Mastcam (Malin, 2013), Navcam (Maki, 2013), and Mars Hand Lens Imager (Edgett, 2013) images used in this manuscript are freely available through the Planetary Data System Cartography and Imaging Sciences. All of the ChemCam Remote Micro-Imager images (Wiens, 2013b) and Laser-Induced Breakdown Spectrometer data (Wiens, 2013a) used in this manuscript are freely available through the Planetary Data System Geosciences node. All 3D Digital Outcrop Models presented in this manuscript are freely accessible for visualization, including in Virtual Reality, on the Sketchfab web-platform (<https://sketchfab.com/LPG-3D>). Complete data tables presented in the Supporting Information of this work are available in the Zenodo open-source online repository (Caravaca et al., 2022).

Acknowledgments

The authors thank Kenneth S. Edgett for constructive discussion and inputs on the treatment of Mars Hand Lens Imager images for photogrammetry. They also gratefully thank the Mars Science Laboratory (MSL) engineering and science teams for all their work on carrying operations and gathering the data used in this work, particularly during the remote work forced by the COVID-19 pandemic. The authors thank the MSL Sedimentology and Stratigraphy Working Group for providing them with a synthetic column of the rover's traverse. Lastly, the authors thank D. W. Mittlefehldt, L. S. Crumpler, and E. Hiatt for their thorough constructive notes that helped to improve this manuscript during the review process. The authors acknowledge the support from the French Agence Nationale de la Recherche (ANR) under the contract ANR-16-CE31-0012 entitled Mars-Prime. This work was supported by the French Space Agency CNES under convention CNES 180027. It is based on observations with ChemCam embarked on *Curiosity*. A part of this work was supported by the National Aeronautics and Space Administration under contracts NNH13ZDA0180 for LANL (R. C. Wiens and N. L. Lanza) and NNH15ZDA001N for participating scientist (C. M. Fedo). S. G. Banham and S. Gupta acknowledge support from the UK Space Agency under grants ST/S001506/1, ST/W002280/1, and ST/S001492/1.

References

- Abercrombie, S. P., Menzies, A., Winter, A., Clausen, M., Duran, B., Jorritsma, M., et al. (2017). OnSight: Multi-platform visualization of the surface of Mars. *AGU Fall Meeting Abstracts*, 2017, ED11C-0134.
- Agisoft LLC. (2020). Metashape Professional (Version 1.6.x). Retrieved from <https://www.agisoft.com/>
- Allen, J. R. L. (1982). *Sedimentary structures, their character and physical basis*. Elsevier Scientific Pub. Co.
- Argast, S., & Donnelly, T. W. (1987). The chemical discrimination of clastic sedimentary components. *Journal of Sedimentary Research*, 57(5), 813–823. <https://doi.org/10.1306/212F8C6F-2B24-11D7-8648000102C1865D>
- Banham, S. G., Gupta, S., Rubin, D. M., Bedford, C. C., Edgar, L. A., Bryk, A. B., et al. (2022). Evidence for fluctuating wind in shaping an ancient Martian dune field: The Stimson formation at the Greenheugh pediment, Gale crater. *Journal of Geophysical Research: Planets*, 127, e2021JE007023. <https://doi.org/10.1029/2021JE007023>
- Banham, S. G., Gupta, S., Rubin, D. M., Edgett, K. S., Barnes, R., Beek, J. V., et al. (2021). A rock record of complex aeolian bedforms in a Hesperian Desert Landscape: The Stimson formation as exposed in the Murray Buttes, Gale crater, Mars. *Journal of Geophysical Research: Planets*, 126(4), e2020JE006554. <https://doi.org/10.1029/2020JE006554>
- Banham, S. G., Gupta, S., Rubin, D. M., Watkins, J. A., Sumner, D. Y., Edgett, K. S., et al. (2018). Ancient Martian aeolian processes and palaeomorphology reconstructed from the Stimson formation on the lower slope of Aeolis Mons, Gale crater, Mars. *Sedimentology*, 65(4), 993–1042. <https://doi.org/10.1111/sed.12469>
- Bedford, C. C., Banham, S. G., Bridges, J. C., Forni, O., Cousin, A., Bowden, D., et al. (2022). An insight into ancient aeolian processes and post-Noachian aqueous alteration in Gale crater, Mars, using ChemCam geochemical data from the Greenheugh capping unit. *Journal of Geophysical Research: Planets*. <https://doi.org/10.1029/2021JE007100>
- Bedford, C. C., Schwenzer, S. P., Bridges, J. C., Banham, S., Wiens, R. C., Gasnault, O., et al. (2020). Geochemical variation in the Stimson formation of Gale crater: Provenance, mineral sorting, and a comparison with modern Martian dunes. *Icarus*, 341, 113622. <https://doi.org/10.1016/j.icarus.2020.113622>
- Bell, J. F., Godber, A., McNair, S., Caplinger, M. A., Maki, J. N., Lemmon, M. T., et al. (2017). The Mars Science Laboratory *Curiosity* rover Mastcam instruments: Preflight and in-flight calibration, validation, and data archiving: MSL/Mastcam calibration. *Earth and Space Science*, 4(7), 396–452. <https://doi.org/10.1002/2016EA000219>
- Bennett, K. A., Fox, V. K., Bryk, A., Dietrich, W., Fedo, C., Edgar, L., et al. (2022). The *Curiosity* rover's exploration of Glen Torridon, Gale crater, Mars: An overview of the campaign and scientific results. *Journal of Geophysical Research: Planets*, 127, e2022JE007185. <https://doi.org/10.1029/2022JE007185>
- Bennett, K. A., & Bell, J. F. (2016). A global survey of Martian central mounds: Central mounds as remnants of previously more extensive large-scale sedimentary deposits. *Icarus*, 264, 331–341. <https://doi.org/10.1016/j.icarus.2015.09.041>
- Bjørlykke, K. (1988). Chapter 2 sandstone diagenesis in relation to preservation, destruction and creation of porosity. In G. V. Chilingarian & K. H. Wolf (Eds.), *Developments in sedimentology* (Vol. 41, pp. 555–588). Elsevier. [https://doi.org/10.1016/S0070-4571\(08\)70180-8](https://doi.org/10.1016/S0070-4571(08)70180-8)
- Bohacs, K. M. (1981). *Flume studies on the kinematics and dynamics of large-scale bedforms* (Doctoral dissertation). Massachusetts Institute of Technology.
- Bristow, T. F., Grotzinger, J. P., Rampe, E. B., Cuadros, J., Chipera, S. J., Downs, G. W., et al. (2021). Brine-driven destruction of clay minerals in Gale crater, Mars. *Science*, 373(6551), 198–204. <https://doi.org/10.1126/science.abg5449>
- Bristow, T. F., Rampe, E. B., Achilles, C. N., Blake, D. F., Chipera, S. J., Crisp, J. A., et al. (2018). Clay mineral diversity and abundance in sedimentary rocks of Gale crater, Mars. *Science Advances*, 4(6), eaar3330. <https://doi.org/10.1126/sciadv.aar3330>
- Cabrol, N. A., Grin, E. A., Newsom, H. E., Landheim, R., & McKay, C. P. (1999). Hydrogeologic evolution of Gale crater and its relevance to the exobiological exploration of Mars. *Icarus*, 139(2), 235–245. <https://doi.org/10.1006/icar.1999.6099>
- Caravaca, G., Le Mouélic, S., Mangold, N., L'Haridon, J., Le Deit, L., & Massé, M. (2020). 3D digital outcrop model reconstruction of the Kimberley outcrop (Gale crater, Mars) and its integration into Virtual Reality for simulated geological analysis. *Planetary and Space Science*, 182, 104808. <https://doi.org/10.1016/j.pss.2019.104808>
- Caravaca, G., Mangold, N., Dehouck, E., Schieber, J., Zaugg, L., Bryk, A. B., et al. (2022). Supplemental data from: "From lake to river: Documenting an environmental transition across the Jura/Knockfarril Hill members boundary in the Glen Torridon region of Gale crater (Mars)" [Dataset]. *Zenodo*. <https://doi.org/10.5281/ZENODO.6364703>
- Chan, M. A., Yonkee, W. A., Netoff, D. I., Seiler, W. M., & Ford, R. L. (2008). Polygonal cracks in bedrock on Earth and Mars: Implications for weathering. *Icarus*, 194(1), 65–71. <https://doi.org/10.1016/j.icarus.2007.09.026>
- Clegg, S. M., Wiens, R. C., Anderson, R., Forni, O., Frydenvang, J., Lasue, J., et al. (2017). Recalibration of the Mars Science Laboratory ChemCam instrument with an expanded geochemical database. *Spectrochimica Acta Part B: Atomic Spectroscopy*, 129, 64–85. <https://doi.org/10.1016/j.sab.2016.12.003>
- Cosgrove, J. W., & Hudson, J. A. (2016). *Structural geology and rock engineering*. World Scientific Publishing Company.
- Cousin, A., Desjardins, M., Dehouck, E., Forni, O., David, G., Berger, G., et al. (2021). K-rich rubbly bedrock at Glen Torridon, Gale crater, Mars: Investigating the possible presence of illite. *LPSC*, XII, 2127.
- David, G., Cousin, A., Forni, O., Meslin, P.-Y., Dehouck, E., Mangold, N., et al. (2020). Analyses of high-iron sedimentary bedrock and diagenetic features observed with ChemCam at Vera Rubin ridge, Gale crater, Mars: Calibration and Characterization. *Journal of Geophysical Research: Planets*, 125(10), e2019JE006314. <https://doi.org/10.1029/2019JE006314>

- Day, M., Anderson, W., Kocurek, G., & Mohrig, D. (2016). Carving intracratere layered deposits with wind on Mars. *Geophysical Research Letters*, *43*(6), 2473–2479. <https://doi.org/10.1002/2016GL068011>
- Dehouck, E., Cousin, A., Mangold, N., Frydenvang, J., Gasnault, O., Forni, O., et al. (2022). Bedrock geochemistry and alteration history of the clay-bearing Glen Torridon region of Gale crater, Mars. *Journal of Geophysical Research: Planets*. <https://doi.org/10.1029/2021JE007103>
- Dehouck, E., Cousin, A., Mangold, N., Frydenvang, J., Gasnault, O., Rapin, W., et al. (2021). Leaving Glen Torridon: Bedrock geochemistry measured by ChemCam en route to the sulfate unit of Gale crater. *LPSC, XII*, 1858.
- Edgar, L. A., Fedo, C. M., Gupta, S., Banham, S. G., Fraeman, A. A., Grotzinger, J. P., et al. (2020). A lacustrine paleoenvironment recorded at Vera Rubin Ridge, Gale crater: Overview of the Sedimentology and stratigraphy observed by the Mars Science Laboratory Curiosity rover. *Journal of Geophysical Research: Planets*, *125*(3), e2019JE006307. <https://doi.org/10.1029/2019JE006307>
- Edgar, L. A., Gupta, S., Rubin, D. M., Lewis, K. W., Kocurek, G. A., Anderson, R. B., et al. (2018). Shaler: *In situ* analysis of a fluvial sedimentary deposit on Mars. *Sedimentology*, *65*(1), 96–122. <https://doi.org/10.1111/sed.12370>
- Edgett, K. S. (2013). MSL Mars Hand Lens Imager 4 RDR image V1.0 [Dataset]. NASA Planetary Data System. <https://doi.org/10.17189/1520292>
- Edgett, K. S., Yingst, R. A., & Fey, D. M. (2020a). Curiosity's Mars Hand Lens Imager (MAHLI) Mars Science Laboratory (MSL) Principal Investigator's Notebook: Sols 2359–2482, version 1 (No. MSL MAHLI Technical Report 0023). <https://doi.org/10.13140/RG.2.2.32038.47685>
- Edgett, K. S., Yingst, R. A., & Fey, D. M. (2020b). Curiosity's Mars Hand Lens Imager (MAHLI) Mars Science Laboratory (MSL) Principal Investigator's Notebook: Sols 2483–2579, version 1 (No. MSL MAHLI Technical Report 0024). <https://doi.org/10.13140/RG.2.2.19355.90400>
- Edgett, K. S., Yingst, R. A., Ravine, M. A., Caplinger, M. A., Maki, J. N., Ghaemi, F. T., et al. (2012). Curiosity's Mars Hand Lens Imager (MAHLI) investigation. *Space Science Reviews*, *170*(1), 259–317. <https://doi.org/10.1007/s11214-012-9910-4>
- Farmer, J. D., & Des Marais, D. J. (1999). Exploring for a record of ancient Martian life. *Journal of Geophysical Research*, *104*(E11), 26977–26995. <https://doi.org/10.1029/1998JE000540>
- Fedo, C. M., Bryk, A. B., Edgar, L. A., Bennett, K. A., Fox, V. K., Dietrich, W. E., et al. (2022). Geology and stratigraphic correlation of the Murray and Carolyn Shoemaker formations across the Glen Torridon region, Gale crater, Mars. *Journal of Geophysical Research: Planets*, *127*, e2022JE007408. <https://doi.org/10.1029/2022JE007408>
- Fedo, C. M., Grotzinger, J. P., Bryk, A., Edgar, L. A., Bennett, K., Fox, V., et al. (2020). Ground-based stratigraphic correlation of the Jura and Knockfarril Hill members of the Murray formation, Gale Crater: Bridging the Vera Rubin ridge – Glen Torridon Divide. *LPSC, XI*, 2345.
- Fedo, C. M., Grotzinger, J. P., Gupta, S., Stein, N. T., Watkins, J., Banham, S., et al. (2017). Facies analysis and basin architecture of the upper part of the Murray formation, Gale crater, Mars. In *48th Annual Lunar and Planetary Science Conference* (p. 1689).
- Fraeman, A. A., Edgar, L. A., Rampe, E. B., Thompson, L. M., Frydenvang, J., Fedo, C. M., et al. (2020). Evidence for a diagenetic origin of Vera Rubin ridge, Gale crater, Mars: Summary and synthesis of Curiosity's exploration campaign. *Journal of Geophysical Research: Planets*, *125*(12), e2020JE006527. <https://doi.org/10.1029/2020JE006527>
- Frydenvang, J., Mangold, N., Wiens, R. C., Fraeman, A. A., Edgar, L. A., Fedo, C. M., et al. (2020). The Chemostratigraphy of the Murray formation and role of diagenesis at Vera Rubin ridge in Gale crater, Mars, as observed by the ChemCam instrument. *Journal of Geophysical Research: Planets*, *125*(9), e2019JE006320. <https://doi.org/10.1029/2019JE006320>
- Garzanti, E., Andó, S., France-Lanord, C., Censi, P., Vignola, P., Galy, V., & Lupker, M. (2011). Mineralogical and chemical variability of fluvial sediments 2. Suspended-load silt (Ganga–Brahmaputra, Bangladesh). *Earth and Planetary Science Letters*, *302*(1), 107–120. <https://doi.org/10.1016/j.epsl.2010.11.043>
- Gasda, P. J., Comellas, J., Essunfeld, A., Das, D., Bryk, A. B., Dehouck, E., et al. (2022). Overview of the morphology and chemistry of diagenetic features in the clay-rich Glen Torridon unit of Gale crater, Mars. *Journal of Geophysical Research: Planets*. <https://doi.org/10.1029/2021je007097>
- Girardeau-Montaut, D. (2020). CloudCompare (Version 2.10). Retrieved from <http://www.cloudcompare.org>
- Goehring, L. (2013). Evolving fracture patterns: Columnar joints, mud cracks and polygonal terrain. *Philosophical Transactions of the Royal Society A: Mathematical, Physical & Engineering Sciences*, *371*(2004), 20120353. <https://doi.org/10.1098/rsta.2012.0353>
- Golombek, M., Grant, J., Kipp, D., Vasavada, A., Kirk, R., Ferguson, R., et al. (2012). Selection of the Mars Science Laboratory landing site. *Space Science Reviews*, *170*(1), 641–737. <https://doi.org/10.1007/s11214-012-9916-y>
- Grotzinger, J. P., Crisp, J., Vasavada, A. R., Anderson, R. C., Baker, C. J., Barry, R., et al. (2012). Mars Science Laboratory mission and science investigation. *Space Science Reviews*, *170*(1), 5–56. <https://doi.org/10.1007/s11214-012-9892-2>
- Grotzinger, J. P., Gupta, S., Malin, M. C., Rubin, D. M., Schieber, J., Siebach, K., et al. (2015). Deposition, exhumation, and paleoclimate of an ancient lake deposit, Gale crater, Mars. *Science*, *350*(6257), aac7575. <https://doi.org/10.1126/science.aac7575>
- Grotzinger, J. P., Milliken, R. E., & SEPM (Society for Sedimentary Geology) (Eds.). (2012). *Sedimentary geology of Mars*. SEPM (Society for Sedimentary Geology).
- Grotzinger, J. P., Sumner, D. Y., Kah, L. C., Stack, K., Gupta, S., Edgar, L., et al. (2014). A habitable fluvio-lacustrine environment at Yellowknife Bay, Gale crater, Mars. *Science*, *343*(6169), 1242777. <https://doi.org/10.1126/science.1242777>
- Gwizd, S., Fedo, C., Grotzinger, J., Edgett, K., Gupta, S., Stack, K. M., et al. (2019). Toward a greater understanding of cross-stratified facies in the Hartmann's Valley member of the Murray formation, Gale crater, Mars. In *Ninth International Conference on Mars* (Vol. 2089, p. 6183).
- Gwizd, S., Fedo, C. M., Grotzinger, J. P., Edgett, K., Rivera-Hernandez, F., & Stein, N. (2018). Grain-size analysis and micro-scale features in Mars Hand Lens imager (Mahli) images from the Hartmann's Valley member, Murray formation, Gale crater, Mars: Links to depositional environment. Presented at the *67th Annual Southeastern GSA Section Meeting – 2018* (p. 312324). <https://doi.org/10.1130/abs/2018SE-312324>
- Hays, L. E., Graham, H. V., Des Marais, D. J., Hausrath, E. M., Horgan, B., McCollom, T. M., et al. (2017). Biosignature preservation and detection in Mars analog environments. *Astrobiology*, *17*(4), 363–400. <https://doi.org/10.1089/ast.2016.1627>
- Hiatt, E. E., & Kyser, T. K. (2000). Links between depositional and diagenetic processes in basin analysis: Porosity and permeability evolution in sedimentary rocks. In *Fluids and basin evolution* (Vol. 28, pp. 63–92).
- Jin, Z., Li, F., Cao, J., Wang, S., & Yu, J. (2006). Geochemistry of Daihai Lake sediments, Inner Mongolia, north China: Implications for provenance, sedimentary sorting, and catchment weathering. *Geomorphology*, *80*(3), 147–163. <https://doi.org/10.1016/j.geomorph.2006.02.006>
- Kah, L. C., Stack, K. M., Eigenbrode, J. L., Yingst, R. A., & Edgett, K. S. (2018). Syndepositional precipitation of calcium sulfate in Gale Crater, Mars. *Terra Nova*, *30*(6), 431–439. <https://doi.org/10.1111/ter.12359>
- L'Haridon, J., Mangold, N., Fraeman, A. A., Johnson, J. R., Cousin, A., Rapin, W., et al. (2020). Iron Mobility during diagenesis at Vera Rubin ridge, Gale crater, Mars. *Journal of Geophysical Research: Planets*, *125*(11), e2019JE006299. <https://doi.org/10.1029/2019JE006299>
- L'Haridon, J., Mangold, N., Meslin, P.-Y., Johnson, J. R., Rapin, W., Forni, O., et al. (2018). Chemical variability in mineralized veins observed by ChemCam on the lower slopes of Mount Sharp in Gale crater, Mars. *Icarus*, *311*, 69–86. <https://doi.org/10.1016/j.icarus.2018.01.028>
- Lazar, O. R., Bohacs, K. M., Macquaker, J. H. S., Schieber, J., & Demko, T. M. (2015). Capturing key attributes of fine-grained sedimentary rocks in outcrops, Cores, and thin sections: Nomenclature and description guidelines. *Journal of Sedimentary Research*, *85*(3), 230–246. <https://doi.org/10.2110/jsr.2015.11>

- Le Deit, L., Hauber, E., Fueten, F., Pondrelli, M., Rossi, A. P., & Jaumann, R. (2013). Sequence of infilling events in Gale Crater, Mars: Results from morphology, stratigraphy, and mineralogy. *Journal of Geophysical Research: Planets*, *118*(12), 2439–2473. <https://doi.org/10.1002/2012JE004322>
- Le Deit, L., Mangold, N., Forni, O., Cousin, A., Lasue, J., Schröder, S., et al. (2016). The potassic sedimentary rocks in Gale crater, Mars, as seen by ChemCam on board *Curiosity*: Potassic sedimentary rocks, Gale crater. *Journal of Geophysical Research: Planets*, *121*(5), 784–804. <https://doi.org/10.1002/2015JE004987>
- Le Mouélic, S., Enguehard, P., Enguehard, P., Schmitt, H. H., Caravaca, G., Seignovert, B., et al. (2020). Investigating Lunar Boulders at the Apollo 17 landing site using photogrammetry and virtual reality. *Remote Sensing*, *12*(11), 1900. <https://doi.org/10.3390/rs12111900>
- Le Mouélic, S., Gasnault, O., Herkenhoff, K. E., Bridges, N. T., Langevin, Y., Mangold, N., et al. (2015). The ChemCam Remote Micro-Imager at Gale crater: Review of the first year of operations on Mars. *Icarus*, *249*, 93–107. <https://doi.org/10.1016/j.icarus.2014.05.030>
- Le Mouélic, S., L'Haridon, J., Civet, F., Mangold, N., Triantafyllou, A., Massé, M., et al. (2018). Using virtual reality to investigate geological outcrops on planetary surfaces. In *EGU General Assembly Conference Abstracts* (p. 13366).
- Loope, D. B., & Burberry, C. M. (2018). Sheeting joints and polygonal patterns in the Navajo Sandstone, southern Utah: Controlled by rock fabric, tectonic joints, buckling, and gullying. *Geosphere*, *14*(4), 1818–1836. <https://doi.org/10.1130/GES01614.1>
- Maki, J., Thiessen, D., Pourangi, A., Kobzeff, P., Litwin, T., Scherr, L., et al. (2012). The Mars Science Laboratory engineering cameras. *Space Science Reviews*, *170*(1), 77–93. <https://doi.org/10.1007/s11214-012-9882-4>
- Maki, J. N. (2013). MSL Mars navigation camera 2 EDV V1.0 [Dataset]. NASA Planetary Data System. <https://doi.org/10.17189/1520295>
- Malin, M. C. (2013). MSL Mars mast camera 4 RDR image V1.0 [Dataset]. NASA Planetary Data System. <https://doi.org/10.17189/1520328>
- Malin, M. C., Caplinger, M. A., Edgett, K. S., Ghaemi, F. T., Ravine, M. A., Schaffner, J. A., et al. (2010). The Mars Science Laboratory (MSL) Mast-mounted cameras (Mastcams) flight instruments. In *41st Annual Lunar and Planetary Science Conference* (p. 1123).
- Malin, M. C., & Edgett, K. S. (2000). Sedimentary rocks of early Mars. *Science*, *290*(5498), 1927–1937. <https://doi.org/10.1126/science.290.5498.1927>
- Malin, M. C., Ravine, M. A., Caplinger, M. A., Tony Ghaemi, F., Schaffner, J. A., Maki, J. N., et al. (2017). The Mars Science Laboratory (MSL) Mast cameras and descent imager: Investigation and instrument descriptions: MSL Mastcam/MARDI descriptions. *Earth and Space Science*, *4*(8), 506–539. <https://doi.org/10.1002/2016EA000252>
- Mangold, N., Forni, O., Dromart, G., Stack, K., Wiens, R. C., Gasnault, O., et al. (2015). Chemical variations in Yellowknife Bay formation sedimentary rocks analyzed by ChemCam on board the *Curiosity* rover on Mars. *Journal of Geophysical Research: Planets*, *120*(3), 452–482. <https://doi.org/10.1002/2014JE004681>
- Mangold, N., Thompson, L. M., Forni, O., Williams, A. J., Fabre, C., Deit, L. L., et al. (2016). Composition of conglomerates analyzed by the *Curiosity* rover: Implications for Gale Crater crust and sediment sources. *Journal of Geophysical Research: Planets*, *121*(3), 353–387. <https://doi.org/10.1002/2015JE004977>
- Maurice, S., Wiens, R. C., Saccoccio, M., Barraclough, B., Gasnault, O., Forni, O., et al. (2012). The ChemCam instrument suite on the Mars Science Laboratory (MSL) rover: Science objectives and Mast unit description. *Space Science Reviews*, *170*(1), 95–166. <https://doi.org/10.1007/s11214-012-9912-2>
- Milliken, R. E., Ewing, R. C., Fischer, W. W., & Hurowitz, J. (2014). Wind-blown sandstones cemented by sulfate and clay minerals in Gale Crater, Mars. *Geophysical Research Letters*, *41*(4), 1149–1154. <https://doi.org/10.1002/2013GL059097>
- Milliken, R. E., Grotzinger, J. P., & Thomson, B. J. (2010). Paleoclimate of Mars as captured by the stratigraphic record in Gale Crater. *Geophysical Research Letters*, *37*(4), L04201. <https://doi.org/10.1029/2009GL041870>
- Nachon, M., Clegg, S. M., Mangold, N., Schröder, S., Kah, L. C., Dromart, G., et al. (2014). Calcium sulfate veins characterized by ChemCam/*Curiosity* at Gale crater, Mars. *Journal of Geophysical Research: Planets*, *119*(9), 1991–2016. <https://doi.org/10.1002/2013JE004588>
- Nachon, M., Mangold, N., Forni, O., Kah, L. C., Cousin, A., Wiens, R. C., et al. (2017). Chemistry of diagenetic features analyzed by ChemCam at Pahrump Hills, Gale crater, Mars. *Icarus*, *281*, 121–136. <https://doi.org/10.1016/j.icarus.2016.08.026>
- O'Connell-Cooper, C. D., Thompson, L. M., Spray, J. G., Berger, J. A., Gellert, R., McCraig, M., et al. (2022). Statistical analysis of APXS-derived chemistry of the clay-bearing Glen Torridon region and Mount Sharp group, Gale crater, Mars. *Journal of Geophysical Research: Planets* [Preprint]. <https://doi.org/10.1002/essoar.10510270.1>
- Ollila, A. M., Newsom, H. E., Clark, B., Wiens, R. C., Cousin, A., Blank, J. G., et al. (2014). Trace element geochemistry (Li, Ba, Sr, and Rb) using *Curiosity*'s ChemCam: Early results for Gale crater from Bradbury landing site to rocknest. *Journal of Geophysical Research: Planets*, *119*(1), 255–285. <https://doi.org/10.1002/2013JE004517>
- Palucis, M. C., Dietrich, W. E., Hayes, A. G., Williams, R. M. E., Gupta, S., Mangold, N., et al. (2014). The origin and evolution of the Peace Vallis fan system that drains to the *Curiosity* landing area, Gale Crater, Mars. *Journal of Geophysical Research: Planets*, *119*(4), 705–728. <https://doi.org/10.1002/2013JE004583>
- Payré, V., Fabre, C., Cousin, A., Sautter, V., Wiens, R. C., Forni, O., et al. (2017). Alkali trace elements in Gale crater, Mars, with ChemCam: Calibration update and geological implications. *Journal of Geophysical Research: Planets*, *122*(3), 650–679. <https://doi.org/10.1002/2016JE005201>
- Rapin, W., Dromart, G., Rubin, D., Deit, L. L., Mangold, N., Edgar, L. A., et al. (2021). Alternating wet and dry depositional environments recorded in the stratigraphy of Mount Sharp at Gale crater, Mars. *Geology*, *49*(7), 842–846. <https://doi.org/10.1130/G48519.1>
- Rapin, W., Ehlmann, B. L., Dromart, G., Schieber, J., Thomas, N. H., Fischer, W. W., et al. (2019). An interval of high salinity in ancient Gale crater lake on Mars. *Nature Geoscience*, *12*(11), 889–895. <https://doi.org/10.1038/s41561-019-0458-8>
- Rapin, W., Meslin, P.-Y., Maurice, S., Vaniman, D., Nachon, M., Mangold, N., et al. (2016). Hydration state of calcium sulfates in Gale crater, Mars: Identification of bassanite veins. *Earth and Planetary Science Letters*, *452*, 197–205. <https://doi.org/10.1016/j.epsl.2016.07.045>
- Rice, M. S., Gupta, S., Treiman, A. H., Stack, K. M., Calef, F., Edgar, L. A., et al. (2017). Geologic overview of the Mars Science Laboratory rover mission at the Kimberley, Gale crater, Mars. *Journal of Geophysical Research: Planets*, *122*(1), 2–20. <https://doi.org/10.1002/2016JE005200>
- Rivera-Hernández, F., Sumner, D. Y., Mangold, N., Stack, K. M., Forni, O., Newsom, H., et al. (2019). Using ChemCam LIBS data to constrain grain size in rocks on Mars: Proof of concept and application to rocks at Yellowknife Bay and Pahrump Hills, Gale crater. *Icarus*, *321*, 82–98. <https://doi.org/10.1016/j.icarus.2018.10.023>
- Rossi, A. P., Neukum, G., Pondrelli, M., vanGasselt, S., Zegers, T., Hauber, E., et al. (2008). Large-scale spring deposits on Mars? *Journal of Geophysical Research*, *113*(E8), E08016. <https://doi.org/10.1029/2007JE003062>
- Rudolph, A., Horgan, B., Bennett, K., Fox, V., Seeger, T., Rice, M., et al. (2020). In situ Mastcam multispectral analysis of clay-rich sediments in the Glen Torridon region of Mt. Sharp, Gale crater, Mars. In *51st Annual Lunar and Planetary Science Conference* (p. 1189).
- Sawyer, E. W. (1986). The influence of source rock type, chemical weathering and sorting on the geochemistry of clastic sediments from the Quetico Metasedimentary Belt, Superior Province, Canada. *Chemical Geology*, *55*(1), 77–95. [https://doi.org/10.1016/0009-2541\(86\)90129-4](https://doi.org/10.1016/0009-2541(86)90129-4)
- Schieber, J., Bish, D., Coleman, M., Reed, M., Hausrath, E. M., Cosgrove, J., et al. (2017). Encounters with an unearthy mudstone: Understanding the first mudstone found on Mars. *Sedimentology*, *64*(2), 311–358. <https://doi.org/10.1111/sed.12318>

- Schieber, J., Stein, N., Grotzinger, J. P., Newsom, H., Williams, R., Miniti, M., et al. (2017). A sand-Lens in the upper Murray formation at Gale crater, Mars: A likely lowstand deposit of a dynamic ancient lake. In *48th Annual Lunar and Planetary Science Conference* (p. 2311).
- Schieber, J., Sumner, D., Bish, D., Stack, K., Miniti, M., Yingst, A., et al. (2015). The Pahrump succession in Gale crater — A potential evaporite bearing lacustrine mudstone with resemblance to Earth analogs. In *Lunar and Planetary Science Conference* (p. 2153).
- Siebach, K. L., Baker, M. B., Grotzinger, J. P., McLennan, S. M., Gellert, R., Thompson, L. M., & Hurowitz, J. A. (2017). Sorting out compositional trends in sedimentary rocks of the Bradbury group (Aeolis Palus), Gale crater, Mars. *Journal of Geophysical Research: Planets*, 122(2), 295–328. <https://doi.org/10.1002/2016JE005195>
- Stack, K. M., Edwards, C. S., Grotzinger, J. P., Gupta, S., Sumner, D. Y., Calef, F. J., et al. (2016). Comparing orbiter and rover image-based mapping of an ancient sedimentary environment, Aeolis Palus, Gale crater, Mars. *Icarus*, 280, 3–21. <https://doi.org/10.1016/j.icarus.2016.02.024>
- Stack, K. M., Grotzinger, J. P., Lamb, M. P., Gupta, S., Rubin, D. M., Kah, L. C., et al. (2019). Evidence for plunging river plume deposits in the Pahrump Hills member of the Murray formation, Gale crater, Mars. *Sedimentology*, 66(5), 1768–1802. <https://doi.org/10.1111/sed.12558>
- Stein, N., Grotzinger, J. P., Schieber, J., Mangold, N., Hallet, B., Newsom, H., et al. (2018). Desiccation cracks provide evidence of lake drying on Mars, Sutton Island member, Murray formation, Gale Crater. *Geology*, 46(6), 515–518. <https://doi.org/10.1130/G40005.1>
- Summons, R. E., Amend, J. P., Bish, D., Buick, R., Cody, G. D., Des Marais, D. J., et al. (2011). Preservation of Martian organic and environmental records: Final report of the Mars Biosignature working Group. *Astrobiology*, 11(2), 157–181. <https://doi.org/10.1089/ast.2010.0506>
- Tavani, S., Granado, P., Corradetti, A., Girundo, M., Iannace, A., Arbués, P., et al. (2014). Building a virtual outcrop, extracting geological information from it, and sharing the results in Google Earth via OpenPlot and Photoscan: An example from the Khaviz Anticline (Iran). *Computers & Geosciences*, 63, 44–53. <https://doi.org/10.1016/j.cageo.2013.10.013>
- Taylor, S. R., & McLennan, S. M. (2009). *Planetary crusts: Their composition, origin and evolution*. Cambridge University Press.
- Thomson, B. J., Bridges, N. T., Milliken, R., Baldrige, A., Hook, S. J., Crowley, J. K., et al. (2011). Constraints on the origin and evolution of the layered mound in Gale Crater, Mars using Mars Reconnaissance Orbiter data. *Icarus*, 214(2), 413–432. <https://doi.org/10.1016/j.icarus.2011.05.002>
- Thorpe, M., Bristow, T., Rampe, E. B., Blake, D. F., Vaniman, D., Yen, A., et al. (2020). Mineralogy of the Glen Torridon region as detailed by the Mars Science Laboratory CheMin Instrument. In *AGU Fall Meeting 2020* (p. P070-03).
- Treiman, A. H., Bish, D. L., Vaniman, D. T., Chipera, S. J., Blake, D. F., Ming, D. W., et al. (2016). Mineralogy, provenance, and diagenesis of a potassic basaltic sandstone on Mars: CheMin X-ray diffraction of the Windjana sample (Kimberley area, Gale crater). *Journal of Geophysical Research: Planets*, 121(1), 75–106. <https://doi.org/10.1002/2015JE004932>
- Triantafyllou, A., Watlet, A., Le Mouélic, S., Camelbeeck, T., Civet, F., Kaufmann, O., et al. (2019). 3-D digital outcrop model for analysis of brittle deformation and lithological mapping (Lorette cave, Belgium). *Journal of Structural Geology*, 120, 55–66. <https://doi.org/10.1016/j.jsg.2019.01.001>
- Ullman, S. (1979). The interpretation of structure from motion. *Proceedings of the Royal Society of London, Series B: Biological Sciences*, 203(1153), 405–426. <https://doi.org/10.1098/rspb.1979.0006>
- Vasavada, A. R., Grotzinger, J. P., Arvidson, R. E., Calef, F. J., Crisp, J. A., Gupta, S., et al. (2014). Overview of the Mars Science Laboratory mission: Bradbury landing to Yellowknife Bay and beyond. *Journal of Geophysical Research: Planets*, 119(6), 1134–1161. <https://doi.org/10.1002/2014JE004622>
- Verhoeven, G. (2011). Taking computer vision aloft – Archaeological three-dimensional reconstructions from aerial photographs with photoscan. *Archaeological Prospection*, 18(1), 67–73. <https://doi.org/10.1002/arp.399>
- Wentworth, C. K. (1922). A scale of grade and class terms for clastic sediments. *The Journal of Geology*, 30(5), 377–392. <https://doi.org/10.1086/622910>
- Westoby, M. J., Brasington, J., Glasser, N. F., Hambrey, M. J., & Reynolds, J. M. (2012). ‘Structure-from-Motion’ photogrammetry: A low-cost, effective tool for geoscience applications. *Geomorphology*, 179, 300–314. <https://doi.org/10.1016/j.geomorph.2012.08.021>
- Wiens, R. C. (2013a). MSL ChemCam laser induced breakdown spectrometer EDR V1.0 [Dataset]. NASA Planetary Data System. <https://doi.org/10.17189/1519439>
- Wiens, R. C. (2013b). MSL Mars ChemCam Remote Micro-Imager camera 5 RDR V1.0 [Dataset]. NASA Planetary Data System. <https://doi.org/10.17189/1519494>
- Wiens, R. C., Blazon-Brown, A. J., Melikechi, N., Frydenvang, J., Dehouck, E., Clegg, S. M., et al. (2021). Improving ChemCam LIBS long-distance elemental compositions using empirical abundance trends. *Spectrochimica Acta Part B: Atomic Spectroscopy*, 182, 106247. <https://doi.org/10.1016/j.sab.2021.106247>
- Wiens, R. C., Maurice, S., Barraclough, B., Saccoccio, M., Barkley, W. C., Bell, J. F., et al. (2012). The ChemCam instrument suite on the Mars Science Laboratory (MSL) rover: Body unit and combined system tests. *Space Science Reviews*, 170(1), 167–227. <https://doi.org/10.1007/s11214-012-9902-4>
- Wiens, R. C., Maurice, S., Lasue, J., Forni, O., Anderson, R. B., Clegg, S., et al. (2013). Pre-flight calibration and initial data processing for the ChemCam laser-induced breakdown spectroscopy instrument on the Mars Science Laboratory rover. *Spectrochimica Acta Part B: Atomic Spectroscopy*, 82, 1–27. <https://doi.org/10.1016/j.sab.2013.02.003>
- Williams, R., & Robinson, D. (1989). Origin and distribution of polygonal cracking of rock surfaces. *Geografiska Annaler – Series A: Physical Geography*, 71(3/4), 145. <https://doi.org/10.2307/521386>